Aalto University
School of Chemical
Technology

**School of Chemical Technology**
**Degree Programme of Process Systems Engineering**

**Pinxiang Han**

# COMPUTATIONAL FLUID DYNAMIC MODELLING OF A PILOT-SCALE BIOREACTOR

**Master's thesis for the degree of Master of Science in Technology submitted for inspection, Espoo, 18 July, 2016.**

**Supervisor** **Professor Ville Alopaeus**

**Instructor** **Ph.D. Robert Spann; Ph.D. Jifeng Yang**

Aalto University
School of Chemical
Technology

Aalto University, P.O. BOX 11000, 00076 AALTO
www.aalto.fi

**Abstract of master's thesis**

| | |
|---|---|
| **Author** | Pinxiang Han |
| **Title of thesis** | Computational fluid dynamic modelling of a pilot-scale bioreactor |
| **Department** | Department of Biotechnology and Chemical Technology |
| **Professorship** | Chemical Engineering |
| **Code of professorship** | KE-42 |
| **Thesis supervisor** | Prof. Ville Alopaeus |
| **Thesis advisor(s) / Thesis examiner(s)** | Ph.D. Robert Spann; Ph.D. Jifeng Yang |
| **Date** | 18.07.2016 |
| **Number of pages** | 74+13 |
| **Language** | English |

**Abstract**

The master's thesis focuses on the investigation of mixing time of a fermentation process using lactic acid bacteria (LAB). Due to the microorganism growth, acid is produced in the process and base is added frequently into the bioreactor for pH control. In this case, gradients of substrate, product and pH might exist in the system. The gradients can result in negative effect on the microorganism growth and process productivity. Thus, it is important to investigate the mixing performance of the bioreactor.

Computational fluid dynamic (CFD) modelling is applied in this thesis to predict fluid flow behavior and mixing time of the pilot-scale bioreactor. The lactic acid bacteria (LAB) fermentation is anaerobic and a one phase CFD model is built based on the pilot-scale bioreactor geometry. The model mesh elements, mesh quality and type and ANSYS CFX settings were studied to get an accurate and reliable CFD model.

Pilot-scale mixing experiments were carried out in order to validate the CFD model. Six pH sensors were mounted on a rack measuring pH at different locations in the bioreactor. Base was added from the top and bottom of the bioreactor at 200rpm and 100rpm impeller speed. pH dynamic data with 1s sampling interval were collected.

CFD simulations were performed at the same conditions as in the pilot experiments. The concentration of tracer at each time step and the calculated mixing time were compared with the pilot experiments for validation.

In the final part of the project, the CFD model is combined a with LAB kinetic model to predict the kinetics of LAB growth and substrate consumption in the bioreactor. The combined CFD and kinetic model was compared at 200rpm, 100rpm and without the fluid flow fields.

**Keywords** Computational fluid dynamics, lactic acid bacteria fermentation, mixing time, pH gradient, pilot-scale bioreactor

# Acknowledgements

I would like to thank my supervisor Ville Alopaeus for his support during the Thesis. I would also like to thank professor Krist V. Gernaey and associate professor Ulrich Krühne from the Technical University of Denmark for offering me this thesis opportunity.

I would like to thank my thesis advisor PhD students Robert Spann and Jifeng Yang from the DTU CAPEC-PROCESS research center. Their guidance, advice and invaluable feedback are highly appreciated.

In addition, I would like to thank David Kold from Chr.Hansen for his great support during the pilot experiments.

Sincerely, I appreciate my family for their support all through the years and their understanding and encouragement when required.

Pinxiang Han
Espoo, Finland, 18 July 2016

# Contents

# List of Figures

# List of Tables

# Nomenclature

| Greek symbol | Description |
|---|---|
| $\beta$ | Response surface parameter |
| $\boldsymbol{\delta}$ | Unit tensor |
| $\delta_n$ | Nitrogen substrate consumption constant |
| $\epsilon$ | Turbulence dissipation rate |
| $\mu$ | Molecular (dynamic) viscosity |
| $\mu_G$ | Growth rate |
| $\mu_{max}$ | Maximum growth rate |
| $\mu_t$ | Turbulent viscosity |
| $\boldsymbol{\pi}$ | Molecular momentum flux tensor |
| $\rho$ | Density |
| $\sigma_\epsilon$ | $k$-$\epsilon$ turbulence model constant |
| $\sigma_k$ | Turbulence model constant for the k equation |
| $\Phi_{ij}$ | Combined momentum flux tensor y component in the x direction |
| $\boldsymbol{\Phi}$ | Combined momentum flux tensor |
| $\boldsymbol{\tau}$ | Viscous momentum flux tensor |
| $\nabla$ | Nabla operator |

| Latin symbol | Description |
|---|---|
| $A$ | Growth associated production coefficient |
| $B$ | Non-growth associated production coefficient |
| $\boldsymbol{c}$ | Vector of medium concentrations of N substrates |
| $\mathbf{c_e}$ | Exit concentration vector |
| $\mathbf{c_f}$ | Inlet concentration vector |

| Latin symbol | Description |
|---|---|
| $C_0$ | Initial concentration |
| $C_1$ | Kinetic model pH function constant |
| $C_2$ | Kinetic model pH function constant |
| $C_3$ | Kinetic model pH function constant |
| $C_{Hla}$ | Lactic acid concentration |
| $C_{La}$ | Lactate concentration |
| $C_P$ | Product concentration |
| $C_{P_{inh}}$ | Product concentration above which bacteria do not growth |
| $C_S$ | Substrate concentration |
| $C_{SC}$ | Carbon substrate concentration |
| $C_{SN}$ | Nitrogen substrate concentration |
| $C_{\epsilon 1}$ | $k$-$\epsilon$ turbulence model constant |
| $C_{\epsilon 2}$ | $k$-$\epsilon$ turbulence model constant |
| $C_\infty$ | Finalised concentration |
| $C_i^{'}$ | Normalised concentration |
| $C_{t,i}^{'}$ | Normalised concentration of sensor i |
| $D$ | Impeller diameter |
| $\boldsymbol{g}$ | Gravitational acceleration vector |
| $g_i$ | Gravitational acceleration vector component i |
| $k$ | Turbulent kinetic energy |
| $k_P$ | Product inhibition constant |
| $k_{[L^-]}$ | Dissociated lactate inhibition constant |
| $k_{[HL]}$ | Undissociated lactic acid inhibition constant |
| $K_{Hla}$ | Kinetic model lactic acid function constant |
| $K_p$ | Kinetic model product function constant |
| $K_{La}$ | Kinetic model lactate function constant |
| $K_s$ | Limiting substrate concentration |
| $K_{SC}$ | Limiting carbon substrate concentration |
| $K_{SN}$ | Limiting nitrogen substrate concentration |
| $N$ | Agitation speed |
| $pH_c$ | Coded pH |
| $pH_{opt}$ | Optimal pH condition for bacteria |
| $pK_a$ | Acid dissociation constant |
| $P_k$ | Shear production of turbulence |
| $P_{kb}$ | Buoyancy production term |
| $P_{\epsilon b}$ | Buoyancy production term |

| Latin symbol | Description |
|---|---|
| $r_p$ | Lactic acid production rate |
| $\mathbf{r}$ | Production rate vector |
| $R_e$ | Reynolds number |
| $R_{e_{crit}}$ | Critical Reynolds number |
| $\mathbf{S_M}$ | External force vector |
| $t$ | Time |
| $t_m$ | Mixing time |
| $\mathbf{v}$ | Velocity vector |
| $v_i$ | Velocity vector direction i |
| $V$ | Volume |
| $WP_c$ | Coded whey permeate concentration |
| $X$ | Biomass concentration |

# CHAPTER 1

# Introduction

In chemical and biochemical processes, mixing behavior is one of the key factors to ensure the production efficiency and product quality. It is highly desired to predict the hydrodynamic behavior inside bioreactors where substrate, oxygen, pressure, temperature, pH and other gradients might exist. All gradients cause different biological responses due to oscillating conditions in large-scale bioreactors which most often have a negative effect on the cell growth rate and production efficiency. Therefore, simulations of those gradients and combining simulations of the gradients with kinetic models is demanded.

Computational fluid dynamic (CFD) modelling is one of the most widely used tools to study the hydrodynamics and the mixing behaviors in chemical and biochemical processes. CFD is computer-based modelling which provides detailed simulation results of the fluid flow inside the bioreactor. It is based on momentum, energy and mass transfer equations and 3-dimensional models are set up for the domain of interest. The resulting differential equations are solved numerically and several profiles, such as fluid velocity fields, are obtained. The CFD technique has a wide range of applications for different fluids, such as aerodynamics of aircraft and vehicles, hydrodynamics of ships, combustion in engines and turbines and the simulation of the external and internal environment of buildings. In chemical process engineering, CFD is used in the areas of mixing, separation, product design and optimization studies. [1]

In fermentation processes, gradients are created due to insufficient mixing at large-scale. The substrate, oxygen or pH gradients have negative effects on the microorganism growth. The mixing time has to be determined in order to characterize the process and the mixing efficiency. Mixing time is defined as the time to achieve a certain degree of homogeneity in a unit operation vessel [2]. The longer the mixing time, the longer it takes to obtain a homogeneous solution and higher

the gradients that exist in the process. Mixing time is related to the fluid properties, agitation speed and dimensions of the reactor. A number of recirculation zones is generated by the impellers and the mixing efficiency can be improved by this manner. [2]

Due to the significant effects of gradients, research on understanding and simulation of gradients in bioreactors is highly demanded. The objective of this thesis project is to use a computational fluid dynamic model to simulate the flow profile of a 750 L bioreactor. Finally a kinetic model of lactic acid bacteria (LAB) fermentation obtained from literature is combined with the CFD model to simulate the pH gradient.

# CHAPTER 2

# Theoretical background

This chapter describes the theoretical background in relation to the thesis project. Section 2.1 explains the mathematical transport and the definition of the turbulence theories and how the flow problem is set up and solved in ANSYS CFX. The transport theory is studied from the work of Bird, Stewart and Lightfoot (1960) [3] and turbulence model is based on the ANSYS CFX-Solver Theory Guide. Section 2.2 describes mixing time determination. Section 2.3 explains the state of the art of unstructured lactic acid bacteria (LAB) kinetic models and the kinetic model (Aghababaie, Khanahmadi and Beheshti, 2015) which is used in the thesis project [4].

## 2.1 Computational fluid dynamics

This section includes the background of computational fluid dynamics (CFD), how the flow problem is set up and solved. The transport theories and turbulence model are also illustrated.

### 2.1.1 Background

CFD has become a powerful and versatile tool in the chemical and biochemical industries. It is powerful to evaluate the momentum, energy and mass transfer in the process in order to describe the fluid flow. With the development of modern computers, complex iterations and calculations can be performed and accurate solutions can be obtained. Such simulations can help to study the hydrodynamics of mixing processes. The basis of CFD originates from transport process theories,

fluid dynamics and thermodynamics from physics, kinetics and catalysis from chemistry and applied mathematics. These science branches are integrated to analyze and solve the fluid dynamics problems [5].

CFD models reduce cost and time in the product design and development phase significantly. When designing the inner side of a reactor, the CFD model enables the designers to visualize the fluid flow inside the reactor. The mixing behavior can be observed with the velocity color contours. Modifications can be formulated and tested to improve the situation when necessary.

Computational fluid dynamic modelling is based on the conservation laws of mass, energy and momentum in the system. Assumptions are made to simplify the problems. Partial differential equations are formulated and initial and boundary conditions are defined to solve the partial differential equations.

Bird, Stewart and Lightfoot (1960) formulated the fundamental CFD knowledge which combines the momentum, energy and mass transfer phenomena within the mathematical Navier-stokes equations [3]. Differential equations, specified boundary conditions and physical properties of the fluid are provided to analyze problems and obtain solutions. The work of Bird, Stewart and Lightfoot is still considered as standard and fundamental theories for computational fluid dynamics. With the development of modern digital computers, it enables the sophisticated calculations of three-dimensional fields in CFD. Assumptions are made to simplify the problem. Simplification helps to reduce computation time and get better results. [5]

Initially CFD was applied mainly in the aeronautical industry. The flow regimes around the airplane were calculated and the design of the aircraft was modified and optimized [6]. Later, CFD was applied to automobile industries to calculate the internal flow and external flow of combustion engines, and it is also used in mechanical and civil engineering [7].

Middleton, Pierce and Lynch (1986) reported the first three dimensional CFD simulation of a stirred tank reactor in the field of chemical engineering [8]. The CFD model was set up for a 30 L vessel and provided accurate predictions for

reaction yield as a function of impeller speed. The reaction rate was chosen slow enough so that the flow pattern of large-scale characteristics having an effect on the reaction.

After that, more studies were carried out to determine the residence time distribution and to understand its influence on final product quality since the mixing behavior is one of the key factors to achieve success in bioreactors. It is highly desired to predict the hydrodynamic behavior when increasing the size of the bioreactors where strong substrate, pH or oxygen gradients might exist [9]. The bioreactor scale-up also causes a different biological response compared to the laboratory experiment and thereby it has a significant effect on the bioreactor efficiency [10].

The turbulent model which includes two extra differential equations was developed to represent the turbulent properties of the flow. It has played an important role in the application of CFD in predicting reactor mixing behavior [11]. Srinophakun and Jitjaroenchai (2000) reported the predicted mixing behavior of a 1500 liter fermenter by CFD in analyzing the possible ways to improve low production yield [12]. Design parameters, such as turbine diameter, liquid height and rotation speed, were changed to find the best settings. The best results showed 80% increment in velocity profile.

Moilanen, Laakkonen and Aittamma (2005) studied an aerobic fermentation process with CFD modelling and performed validation of a CFD model of a simple laboratory system [13]. The validated models were then used to simulate the industrial scale fermenters. The report included observations of large inhomogeneous areas inside the fermenters. The local reaction and mass transfer conditions needed to be optimized in order to improve the performance. Delafosse et al. (2014) reported a study of a CFD-based compartment model for description of mixing in bioreactors [14]. The CFD model was validated on the basis of experimental data obtained with PIV (Particle Image Velocimetry). In most parts of the reactors, the CFD simulated turbulent velocity agreed quite well with the PIV results. However, discrepancies were observed in the vicinity of the impeller and in the discharge flow.

### 2.1.2 Geometry and mesh generation

There are many CFD software codes available including both open source and commercial ones. For this thesis work, SolidWorks 2015 is used to build the model geometry. ANSYS CFX 16.1 is applied to build the CFD model and solve fluid dynamic simulations. Integrated Computer Engineering and Manufacturing (ICEM CFD) is used as the software tool to make the meshing. CFX-Pre is used to set up model, CFX-Solver to solve dynamic equations and CFX-Post to visualise the obtained results.

The first step to make a CFD model is to define the geometry. The geometry defines the boundaries of the fluid and presents the complexity of the local areas. The geometry is usually built in SolidWorks. For a bioreactor equipped with rotational impellers, it is often necessary to separate the domain into stationary and rotational domains. The rotational speed can be set the same as the impeller speed. In this case, the wall velocity inside the rotational domain is then zero.

After the geometry is defined in SolidWorks, the geometry is imported into ICEM-CFD to make the meshing. The mesh is the collection of computer defined elements covering the domain of the geometry to be modelled. The whole domain is divided into a number of mesh elements. Each mesh element is assigned with its own value for process parameters, such as velocity, pressure and temperature. For each mesh element, the assumptions are made based on the chosen model and the numerical equations are solved individually. Then the calculated data is collected for the entire domain. [15]

There are different ways to make a mesh in ICEM CFD. The two most common methods are four-side tetrahedral unstructured mesh and six-side hexahedral structured mesh. There are also mesh types like pyramidal or prismatic. [15] The unstructured mesh is generated by ICEM CFD more or less automatically. It is convenient when the geometry is complex, however the resulting mesh quality might be poor and it is difficult to optimize the mesh as well. On the other hand, the structured mesh is made manually. It is built by making a blocking and then split and control the blocking so that the nodes of the block can fit to the user

defined position. In this way, the whole geometry can be described. It is quite difficult and time consuming to make a structured mesh when the geometry is complex. But the reliability and accuracy of the structured mesh is better. Figure 2.1 shows a cube with unstructured mesh (left) and structured mesh (right).

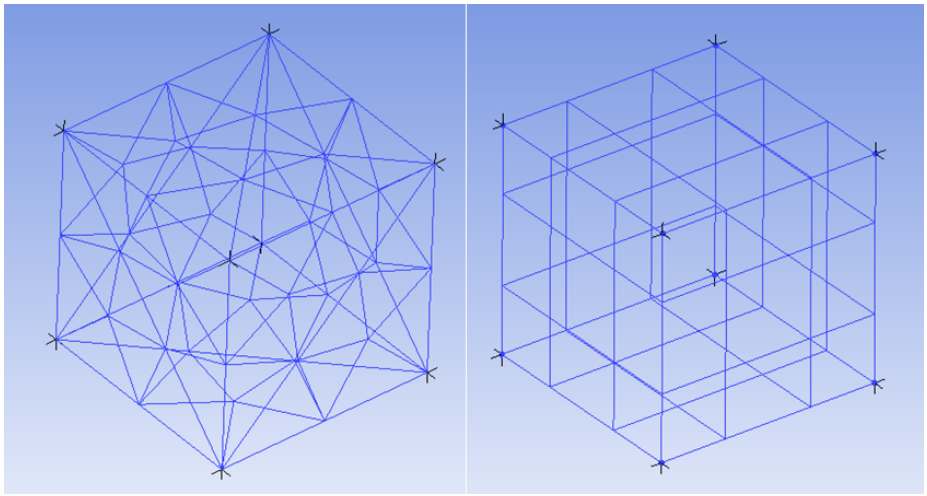

**Figure 2.1:** Unstructured mesh (left) and structured mesh (right).

The quality of the structured mesh can be visualised in the pre-mesh quality histograms in ICEM-CFD. The most common option is to check the minimum angle of the adjacent mesh elements. A good mesh is characterized by the large angle of the neighbouring meshes. These specific areas with low angle should be further optimized.

There are several techniques to improve the structured mesh quality, such as making point and curve association, adding an O-grid for the cylindrical structure and moving vertices to adjust the mesh angle. As a rule of thumb, the structured mesh is acceptable when there is no mesh element with minimum angle less than 9 degrees in the pre-mesh quality histograms, see figure 2.2.

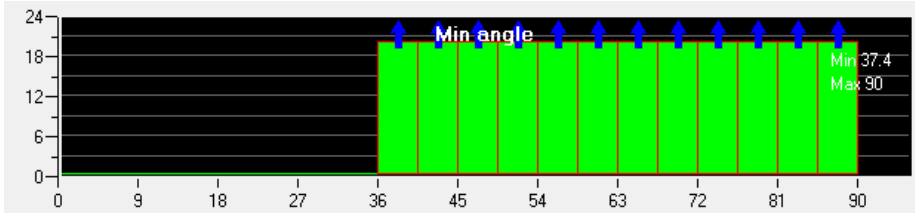


**Figure 2.2:** Mesh minimum angle after optimization.

### 2.1.3 Setting up and solving the flow problem

The flow problem is set up by defining the transport equations to be solved. Input parameters such as fluid properties, boundary conditions and domain settings need to be clarified. When a transient simulation is made, initial conditions, time step and steady state fluid velocities are regarded as inputs as well.

To solve the flow problem, the CFX-solver applies the transport equations to the mesh and obtains numerical solutions. The root mean square (RMS) or maximum (MAX) value of the residual is calculated. The residual can be the velocity component in one direction. The residual target is set by the user and when all the calculated residuals are below the target value, the solver is stopped and the converged solution is obtained. If the converged solution is not obtained or the calculated residuals are fluctuating periodically, it means that the solver cannot find a converged solution. The reasons for that can be poor mesh quality, wrong CFX-pre settings or there is no actual steady state for the flow problem. [16]

After the converged solution is obtained, the result is imported to CFX-Post for post processing. The calculated variables in each mesh cell can be visualised by making a contour on the user-defined plane.

### 2.1.4 Transport equations

CFD is a computer-aided simulation tool solving momentum, heat and mass transfer balances. After the partial differential equations are derived, they are discretized and solved numerically. In the commercial code CFX, the finite volume method is used to divide the region of interest into a number of control volumes. The discretized equations are solved for each control volume iteratively.

[17]

The fundamental equations involved in CFD are known as continuity and momentum equations. The continuity equation is developed by writting a mass balance over a volume element $\Delta x \Delta y \Delta z$ in the Cartesian coordinates, see figure 2.3 [3].

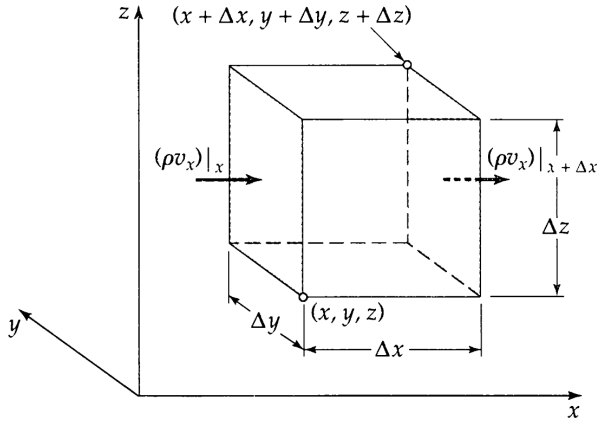


**Figure 2.3:** Fixed volume element [3].

On the x-axis, the rate of mass entering the volume element through the face x is $(\rho v_x)\big|_x \Delta y \Delta z$. The rate of mass leaving the face $x + \Delta x$ is $(\rho v_x)\big|_{x+\Delta x} \Delta y \Delta z$. Similar terms can be derived for the y and z axis. The rate of mass increase within the volume element is $\Delta x \Delta y \Delta z (\frac{\partial \rho}{\partial t})$. This gives the mass balance equation 2.1.

$$\Delta x \Delta y \Delta z \frac{\partial \rho}{\partial t} = \Delta y \Delta z [(\rho v_x)\big|_x - (\rho v_x)\big|_{x+\Delta x}] + \Delta z \Delta x [(\rho v_y)\big|_y - (\rho v_y)\big|_{y+\Delta y}] + \Delta x \Delta y [(\rho v_z)\big|_z - (\rho v_z)\big|_{z+\Delta z}] \quad (2.1)$$

After dividing both sides by $\Delta x \Delta y \Delta z$ and taking limit of $\Delta x$, $\Delta y$, $\Delta z$ to zero we get

$$\frac{\partial \rho}{\partial t} = -(\frac{\partial}{\partial x}\rho v_x + \frac{\partial}{\partial y}\rho v_y + \frac{\partial}{\partial z}\rho v_z) \quad (2.2)$$

The left side of equation 2.2 is the rate of increase of mass per unit volume and

the right side is the net rate of mass addition per unit volume by convection. The continuity equation can also be written as

$$\frac{\partial \rho}{\partial t} + (\nabla \cdot \rho v) = 0 \tag{2.3}$$

Assuming an incompressible fluid with constant density, the continuity equation can be simplified as

$$(\nabla \cdot \rho v) = 0 \tag{2.4}$$

The equation of motion is developed by writing a momentum balance over the volume element $\Delta x \Delta y \Delta z$ in figure 2.3. The combined momentum flux tensor $\mathbf{\Phi}$ which is the sum of the convective momentum flux tensor $\rho \mathbf{vv}$ and the molecular momentum flux tensor $\boldsymbol{\pi}$ is used to describe the momentum transfer in the system.

The rate of the x-component combined momentum flux entering through the face $x$ is $(\Phi_{xx})\big|_x \Delta y \Delta z$ and the rate leaving at $x + \Delta x$ is $(\Phi_{xx})\big|_{x+\Delta x} \Delta y \Delta z$. The rate of x-component which enters through face $y$ is $(\Phi_{yx})\big|_y \Delta z \Delta x$ and the rate of the x-component which leaves through face $y + \Delta y$ is $(\Phi_{yx})\big|_{y+\Delta y} \Delta y \Delta z$. Similarly, we get the rate of x-component which enters and leaves through face $z$ and $z + \Delta z$ are $(\Phi_{zx})\big|_z \Delta x \Delta y$ and $(\Phi_{zx})\big|_{z+\Delta z} \Delta x \Delta y$. After adding the external force which is the gravitational force, we get the net rate of combined momentum change of the x-component as

$$\Delta y \Delta z((\Phi_{xx})\big|_x - (\Phi_{xx})\big|_{x+\Delta x}) + \Delta z \Delta x((\Phi_{yx})\big|_y - (\Phi_{yx})\big|_{y+\Delta y}) + \Delta x \Delta y((\Phi_{zx})\big|_z - (\Phi_{zx})\big|_{z+\Delta z}) + \rho g_x \Delta x \Delta y \Delta z$$

The above part is equal to the rate of momentum increase within volume element $\Delta x \Delta y \Delta z(\frac{\partial \rho v_x}{dt})$. By dividing both sides by $\Delta x \Delta y \Delta z$ and taking the limit as $\Delta x$, $\Delta y$, $\Delta z$ go to zero we get

$$\frac{\partial}{\partial t} \rho v_x = -(\frac{\partial}{\partial x} \Phi_{xx} + \frac{\partial}{\partial y} \Phi_{yx} + \frac{\partial}{\partial z} \Phi_{zx}) + \rho g_x \tag{2.5}$$

Similarly, we can derive the y- and z-component momentum balance, equation 2.6 and 2.7.

$$\frac{\partial}{\partial t}\rho v_y = -(\frac{\partial}{\partial x}\Phi_{xy} + \frac{\partial}{\partial y}\Phi_{yy} + \frac{\partial}{\partial z}\Phi_{zy}) + \rho g_y \tag{2.6}$$

$$\frac{\partial}{\partial t}\rho v_z = -(\frac{\partial}{\partial x}\Phi_{xz} + \frac{\partial}{\partial y}\Phi_{yz} + \frac{\partial}{\partial z}\Phi_{zz}) + \rho g_z \tag{2.7}$$

After combining equation 2.5, 2.6 and 2.7 vectorially, we get

$$\frac{\partial}{\partial t}\rho \mathbf{v} = -[\nabla \cdot \mathbf{\Phi}] + \rho \mathbf{g} \tag{2.8}$$

The combined momentum flux tensor $\mathbf{\Phi}$ can be constituted by the convective momentum flux tensor $\rho\mathbf{vv}$ and the molecular momentum flux tensor $\boldsymbol{\pi}$ by $\mathbf{\Phi} = \rho\mathbf{vv} + p\boldsymbol{\delta} + \boldsymbol{\tau}$. The general term of external force $\mathbf{S_M}$ replaces the gravitational force and we get the equation of motion in equation 2.9.

$$\frac{\partial}{\partial t}\rho \mathbf{v} = -[\nabla \cdot \rho\mathbf{vv}] - \nabla p - [\nabla \cdot \boldsymbol{\tau}] + \rho \mathbf{g} \tag{2.9}$$

In the equation of motion 2.9, the left term is the rate of increase of momentum per unit volume. The terms on the right-hand side are the sum of the rate of momentum addition by convection and molecular transport and external force per unit volume.

[3]

### 2.1.5 Turbulence and $k$-$\epsilon$ model

Turbulent flow motion is unsteady and the flow behavior is random and chaotic. Velocity and pressure change continuously with time in the region of interest. The Reynolds number $R_e$ is the dimenstionless quantity for fluid flow characterisation. In the engineering practice, the Reynolds number $R_e$ is important to characterize the inertia and viscous forces of fluid flow. Laminar flow refers to the flow with Reynolds number $R_e$ below 2300. The flow is smooth and adjacent layers flow in order with each other. When $R_e$ is between 2300 and 4000, the flow is called transient flow. Turbulent flow is defined when $R_e$ is above 4000. Turbulence occurs when the fluid flow inertia force becomes significant compared to the viscous force. [1]

The Navier-Stokes equations are able to describe the laminar and turbulent flow theoretically. However, the Reynolds number in turbulent flow varies from a large range of turbulent length and time scales. In reality, the turbulent length scales can be much smaller than the smallest finite volume mesh element in numerical analysis. [18]

A number of turbulent models have been developed in CFD code to represent the effects of turbulence without a prohibitively fine mesh or direct numerical simulation, such as Reynolds averaged Navier-Stokes (RANS) equations, eddy viscosity turbulence model and the two equation $k$-$\epsilon$ model.

The RANS equations introduces averaged and fluctuating components to the transport equations. In this way, the relatively large time scale is able to solve the equations in turbulent fluctuations. The eddy viscosity turbulence model is based on the hypothesis that the Reynolds stresses from the RANS equations are related to the mean velocity gradients and turbulent viscosity is related to the gradient diffusion hypothesis. The turbulent fluctuations are then expressed using functions of eddy viscosity and eddy diffusivity. [18]

The two equation $k$-$\epsilon$ model is considered to be stable and numerically robust. It gives high accuracy and predictive capability. The model uses turbulent kinetic energy $k$ and turbulence dissipation rate $\epsilon$ to compute the turbulence velocity scale. $k$ and $\epsilon$ are obtained from the differential transport equations for turbulence kinetic energy and dissipation rate, see equation 2.10 and equation 2.11. [18]

$$\frac{\partial}{\partial t}(\rho k) + \frac{\partial}{\partial x_j}(\rho v_j k) = \frac{\partial}{\partial x_j}[(\mu + \frac{\mu_t}{\sigma_k})\frac{\partial k}{\partial x_j}] + P_k - \rho\epsilon + P_{kb} \tag{2.10}$$

$$\frac{\partial}{\partial t}(\rho \epsilon) + \frac{\partial}{\partial x_j}(\rho v_j \epsilon) = \frac{\partial}{\partial x_j}[(\mu + \frac{\mu_t}{\sigma_\epsilon})\frac{\partial \epsilon}{\partial x_j}] + \frac{\epsilon}{k}(C_{\epsilon 1}P_k - C_{\epsilon 2}\rho\epsilon + C_{\epsilon 1}P_{\epsilon b}) \tag{2.11}$$

$P_k$ is the turbulence production due to viscous forces as

$$P_k = \mu_t[\frac{\partial v_i}{\partial x_j} + \frac{\partial v_j}{\partial x_i}]\frac{\partial v_i}{\partial x_j} - \frac{2}{3}\frac{\partial v_k}{\partial x_k}[3\mu_t\frac{\partial v_k}{\partial x_k} + \rho k] \tag{2.12}$$

In this case, the flow turbulence velocity scale is described by the turbulent kinetic energy $k$ and the turbulence dissipation rate $\epsilon$. The description for all constant parameters can be found in the section Nomenclature. [18]

## 2.2 Bioreactor and mixing time determination

The working principles of fermentation and bioreactor, and how the mixing time is determined are explained in this section.

### 2.2.1 Fermentation and bioreactor

Fermentation processes have been invented long time ago. Beer, wine, tofu and cheese are all produced by bioprocesses through fermentation. Some of the well-established techniques are still playing important roles in modern fermentation processes. In fermentation processes, products like antibiotics, vitamins, chemicals, steroids and lactic acid are produced. One of the advantages of fermentation processes is that they consume generally less energy compared to other approaches [19]. Fermentation is achieved by cultivation of a high amount of microorganisms in a dedicated vessel. The vessel to carry out the fermentation is called a bioreactor or a fermenter [20]. While the chemical engineers contributed their knowledge into reaction engineering, mixing and process optimization, biologists deal with the problems mainly related to the organisms to be cultivated [19].

A bioreactor is designed to provide the optimum conditions for the growth of the organisms. The bioreactor is usually a cylindrical vessel with a hemisphere top or bottom. The size range of bioreactors differs from microscale bioreactor, laboratory scale bioreactor, pilot-scale bioreactor and industrial scale bioreactor. Since microorganisms are sensitive and unstable, bioreactors have to maintain the desired conditions in order to avoid loss of productivity. [20]

Fermentation processes are classified as batch, fed-batch and continuous fermentation, as shown in the figure 2.4. In the batch fermentation, all the nutrients are added only once at the beginning. Additives such as acid or base for pH control and antifoam agent can be added during the batch processes. One of

the disadvantages of batch fermentations is that the cell growth rate is often limited by low substrate or high inhibitor concentrations. In continuous processes, on the other hand, nutrients are supplied continuously, and product flow leaves the bioreactor continuously as well. The outlet flow is controlled so that the liquid volume inside the fermenter is kept constant. In a fed-batch processes, a concentrated solution of one medium component is supplied. The medium component can be carbon or any energy source. In the fed-batch processes, there is no outflow so the liquid volume in the fermenter is continuously increasing. [10]

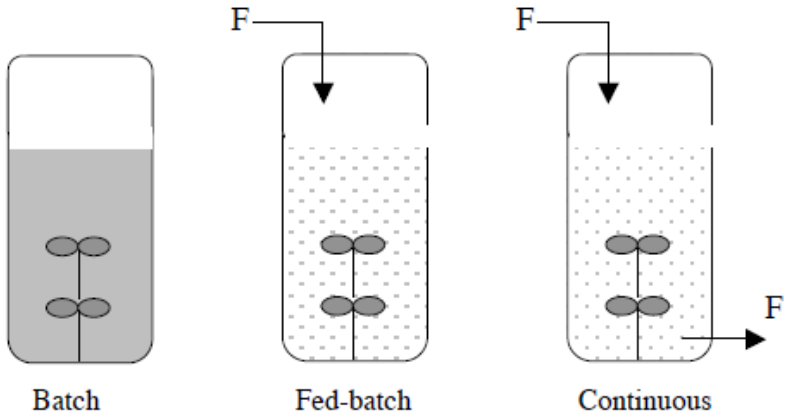


**Figure 2.4:** Three main fermentation processes [10].

In fermentation processes, the nutrition source is referred as the medium and an individual component from the medium is called substrate. The initial cells added in the beginning of the fermentation processes is called biomass. [21]

A bioreactor is used in fermentation processes to cultivate the cells and provide the optimum conditions for the cell growth. A fermentation can be classified into two types, anaerobic and aerobic fermentation. Anaerobic fermentation works in absence of oxygen while in the aerobic process microorganisms require oxygen for respiration and it is supplied by continuous aeration.

### 2.2.2 Mixing time determination

Mixing is the process in order to achieve homogeneity and eliminate gradients in the system. In large-scale reactors, the mixing is so important that it can have

a big influence on the performance of process. In terms of bioprocesses, mixing is important for achieving homogeneity of substrates and biomass concentrations throughout the bioreactor. When substrate, oxygen or pH gradients exist, loss of productivity might occur in the process. [2]

Poor mixing has a significant influence on the fermentation process efficiency. Regardless of whether an aerobic or an anaerobic fermentation process is studied, one of the key factors to achieve success is the mixing efficiency in the bioreactor. During mixing, the medium or biomass from the liquid phase or oxygen from the gas phase reaches the same concentration at every point in the reactor [22]. Mechanical energy is applied in the mixing processes to achieve homogeneity with one or more stirred impellers and with wall-mounted baffles. A typical stirred tank bioreactor is shown in the figure 2.5.

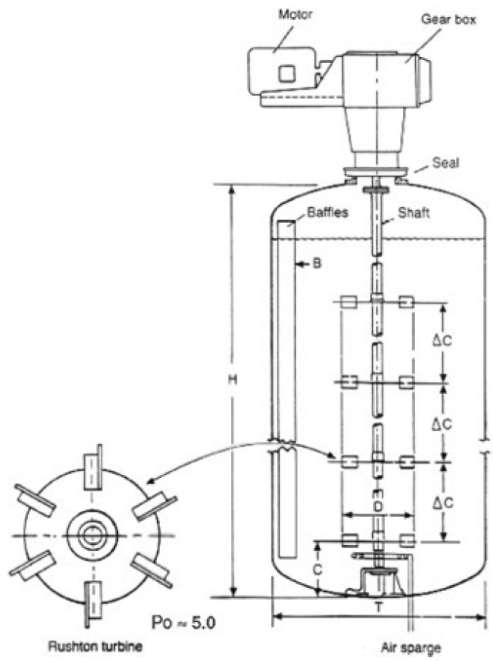


**Figure 2.5:** Typical Stirred Tank Bioreactor [22].

One or more impellers are mounted on a shaft. The impeller creates axial and radial flow patterns when rotating. The flow movements homogenize the substrate

and biomass and enhance the mixing efficiency. Two typical types of turbines, Rushton turbines and axial turbines are shown in the figure 2.6. Rushton turbines are designed as a flat disk mounted with vertical blades and was very often used in early bioreactors. Axial turbines equip inclined impellers which creates both axial and radial flow. The axial impellers are often combined with radial ones to enhance mixing. Baffles are commonly installed with a short distance to the tank wall to create turbulence when the circular flow passes by and avoid a vortex in the bioreactor. [19]

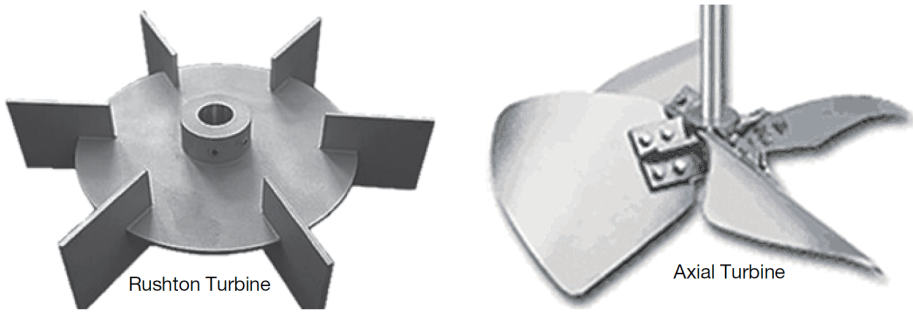


**Figure 2.6:** Rushton and axial turbine [19].

Insufficient mixing can reduce the product yield or product quality. Too high or too low concentration regions of substrate are not preferred for the biomass growth. As the organisms releases acid during growth in the fermentation process, the pH decreases continuously and when the pH is below the cell's preferred pH range, cell activity, fermentation yield and product quality are significantly affected. Growth kinetics of the bacteria and physiological state are strongly influenced by process parameters like pH. In order to control the pH and maintain the optimum pH range, base such as ammonia is added frequently at one point of the process. The pH control can improve various growth characteristics such as specific growth rate, fermentation efficiency and maximum biomass concentration. The mixing of ammonia has to be studied to ensure there is no pH gradient. The occurrence of a pH gradient could also influence the microorganism activity and reduce fermentation efficiency. [23]

Mixing performance can be described as the ability of flow patterns to sweep the entire bioreactor and deliver the substrates, biomass or oxygen to the most

remote areas with efficient energy. Turbulence is essential in order to achieve sufficient mixing. The mixing is a combination of distribution, dispersion and diffusion. Distribution is the process where the bulk fluid flow transports the substrates around the bioreactor. The rotation speed can increase the distribution rate significantly. Distribution is also enhanced when more turbulence is created. This is because the fluid pattern does not travel along the streamlines but moves erratically. Dispersion refers to the process that the fluid is broken down into small eddies. Small eddies are created by stirring and possess kinetic energy. Dispersion facilitates the mass transfer in the bioreactor and the effect is limited by the eddy sizes. Diffusion refers to the molecular transfer in the fluid. Molecular diffusion is accomplished rapidly in the small distances. [2]

Mixing time is a common parameter to assess the mixing efficiency and it refers to the time required to achieve a degree of homogeneity in a vessel. The mixing time varies with the fluid properties, agitation speed and size of the reactor. The relationship has been determined experimentally for a vessel equipped with a Rushton turbine according to equation 2.13. [2]

$$Nt_m = \frac{1.54V}{D^3} \tag{2.13}$$

The Reynolds number $R_e$ which represents the fluid characteristics has a big impact in the low Reynolds numbers region ($R_e$ below 5000).

$$R_e = \frac{ND^2\rho}{\mu} \tag{2.14}$$

Usually mixing time is measured by injecting a base, acid or salt solution tracer into the reactor and measure the concentration as a function of time in fixed points. Ascanio (2015) reviewed different techniques for mixing time determination. Based on the level of disturbance to the flow, the techniques can be classified as non-intrusive and intrusive. Non-intrusive techniques are colorimetry, electrical resistance tomography, positron emission particle tracking, planar laser induced fluorescence and thermography. Compared to non-intrusive techniques, the intrusive techniques like pH and conductivity are accurate but the disadvantage is that the flow pattern is modified due to the presence of the probes. [24]

pH is defined as the negative logarithm of the hydrogen ion concentration. It is the measurement of acidity or alkalinity in a solution and measured by pH electrodes. A pH sensor consists of two parts, a measuring electrode and a reference electrode. Calibration is necessary periodically to make sure that the pH sensor is working properly. [25]

Conductivity is defined as the ability of the material to pass an electric current. In solutions, the current is carried by cationic and anionic ions. A typical conductivity probe consists of an anode and cathode. Conductivity is measured by applying electrical current and measuring the resulting voltage. [26]

pH and conductivity techniques are both instructive and favorable for large scale where effect of probes on the flow pattern is negligible compared to the bulk flow. pH and conductivity are both measurements which can be converted to concentration data and plotted as a function of time. However, the response time (aounrd 4s) needs to be included with the pH measurement due to the thickness of the glass. For conductivity, the response time is less (less than 3s [27]) but the temperature need to be kept constant as the conductivity of a solution is sensitive to temperature. [24, 25]

In the thesis project, Endress+Hauser ion-sensitive field effort transistors (ISFET) pH sensors are used in the pilot-scale experiments. The basic principle of the sensor is shown in the figure 2.7. The medium (pos. 4) is contacted directly with the gate isolator layer (pos. 3). The gate works as an ion-selective layer for $H^+$ ions. In the semiconductor material (pos. 5), two N-conducting areas (pos. 2) are formed. On the left, the Source (S) supplies current and on the right, the Drain (D) accepts current. A current is induced due to the electron density difference. The potential between the gate and source is then calculated from the reference electrode (pos. 1) and converted to the concentration of the $H^+$ ions. [28]

The data obtained from the pH sensor has to be normalized in order to determine the characteristic mixing time. The pH data is first converted to $H^+$ ion concentration. One initial concentration before adding the tracer $C_0$ and one final

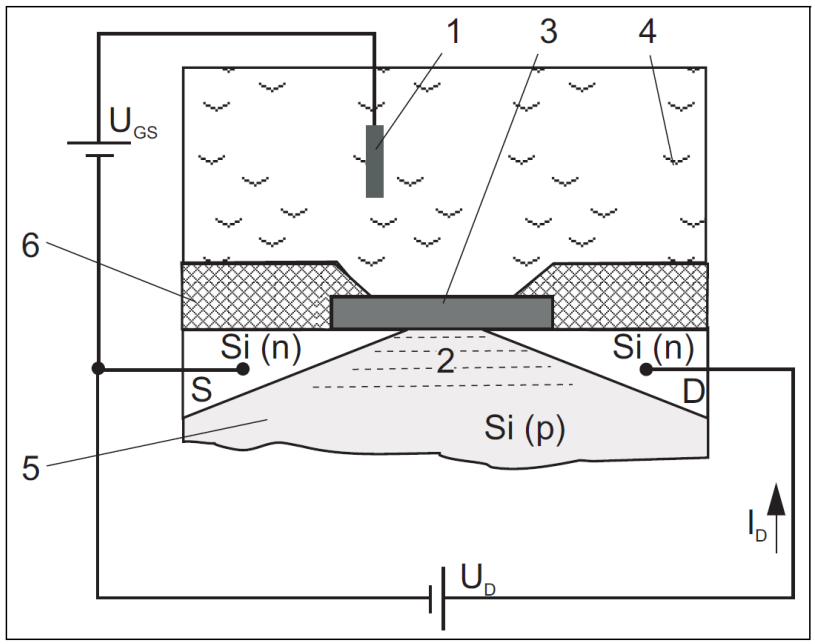


**Figure 2.7:** Principle of ISFET pH sensor [28].

concentration after the concentration of the tracer is stable are used to calculate the normalized value as in equation 2.15 [29].

$$C_i' = \frac{C_i - C_0}{C_\infty - C_0} \tag{2.15}$$

As the sensor fluctuation decays exponentially, the data is then plotted as log variance as a function of time as in equation 2.16 [29].

$$\log \sigma^2 = \log(C_t' - 1) \tag{2.16}$$

95% of mixing is achieved at the time when $C' = 0.95$. All the sensors need to be combined to calculate the overall mixing time of the system. RMS variance is calculated from equation 2.17 [29].

$$\log \sigma_{RMS}^2 = \log \left\{ \frac{1}{n} \sum_{i=1}^{n} (C_{t,i}' - 1)^2 \right\} \tag{2.17}$$

where $C_{t,i}'$ is the normalised concentration of sensor i.

Delvigne, Destain and Thonart (2006) studied the mixing time of a 500L and a 2000L bioreactors under varying operating conditions (agitation speed and impeller combination) [30]. The mixing time is calculated at 85% mixedness. The experimental mixing time is summarised in table 2.1.

Mixing time is important to evaluate how long it takes for the system to achieve homogeneity. With measurement of pH sensors, the mixing time of the bioreactor can be determined and calculated from the experimental data.

## 2.3 Lactic acid bacteria (LAB) kinetic model

The general state of the art of unstructured kinetic models and the LAB model used in this thesis project are described in this section.

### 2.3.1 LAB fermentation

Lactic acid bacteria fermentation has been development long time ago. Dairy products such as yoghurt, cheese, buttermilk are all preserved by acid produced due to bacterial activity. Lactic acid improves the flavor, storage quality and the amount of probiotics. [31]

The microorganism that produce lactic acid are known as Lactic acid bacteria (LAB). They convert carbohydrates to lactic acid. LAB have wide applications in the chemical, biochemical and pharmaceutical industries. For centuries, they have been used in the milk fermentation process in dairy production. The fermented milk products such as cheese and yoghurt take approximately 20% of the fermented food production in the world. [32]

LAB convert lactose in the milk into lactic acid which gives a fresh acid flavor. LAB are also helpful in terms of lipolytic activity and maturation of ripened dairy products. Lactic acid bacteria can be classified as heterofermentative and homofermentative. Homofermentative LAB like streptococci produces lactic acid as the only product. Heterofermentative LAB such as leuconostocs produces

**Table 2.1:** Mixing time of 500L and 2000L scale bioreactors.

| Reactor | Working volume (L) | Impeller | Agitation speed ($s^{-1}$) | Mixing time 85% (s) |
|---|---|---|---|---|
| Bioreactor 500L | 350 | Two Rushton turbines | 0.83 | 36 |
| Bioreactor 500L | 350 | Two Rushton turbines | 1.66 | 34 |
| Bioreactor 500L | 350 | Two Rushton turbines | 2.5 | 22 |
| Bioreactor 500L | 350 | Two Rushton turbines | 3.33 | 20 |
| Bioreactor 2000L | 1200 | Two Rushton turbines | 0.63 | 60 |
| Bioreactor 2000L | 1200 | Two Rushton turbines | 1.2 | 42 |
| Bioreactor 2000L | 1200 | Two Rushton turbines | 1.81 | 26 |
| Bioreactor 2000L | 1200 | Two Rushton turbines | 2.36 | 26 |
| Bioreactor 2000L | 1800 | Three Rushton turbines | 0.63 | 188 |
| Bioreactor 2000L | 1800 | Three Rushton turbines | 1.2 | 100 |
| Bioreactor 2000L | 1800 | Three Rushton turbines | 1.81 | 52 |
| Bioreactor 2000L | 1800 | Three Rushton turbines | 2.36 | 53 |

carbon dioxide, acetic acid and ethanol in addition to lactic acid. This project focuses on homofermentative Streptococcus thermophiles. [32]

### 2.3.2 Unstructured LAB kinetic models

Kinetic models are used to describe the microbial process during the fermentation. The reactions are described by a number of ordinary or partial differential equations. The dynamics of the studied processes can be obtained from the solutions. The size of the kinetic reaction networks depends on the number of equations and the complexity of the phenomena to be described. [33]

In order to define the model structure, the stoichiometry of the reactions has to be considered. The stiochiometry describes the amount of substrates taken up by the cell, metabolic products produced and biomass constituents formed in intracellular reactions. The general mass balance of the bioreactor is set up in order to calculate the reaction rate for different components. Differential equations for biomass, substrate and product concentration dynamics are derived. The biological reaction rate model is developed to describe the organism growth rate under the influence of the external environment. Environmental conditions like pH, temperature, substrate concentration or inhibitor concentration have an effect on the cell specific growth rate. However, only operating parameters like pH and temperature can be monitored and controlled. Kinetic models are in gerenal applied for understanding, designing and controlling the fermentation processes. [4]

The kinetic models can be classified as unstructured, structured, non-segregated and segregated models. In a segregated model, different cell populations are described. The unstructured model doesn't include the variations of intracellular properties. The unstructured model is mainly used for steady state or quasi-steady modelling [10]. Here a general description of an unstructured LAB kinetic model is provided.

The microorganisms growth kinetics is described with equation 2.18.

$$\frac{dX}{dt} = \mu_G \cdot X \tag{2.18}$$

There are models which also include the cell death in the growth kinetic model. Here it is omitted since the death rate does not play a crucial role in batch operation.

The specific growth rate µ can be limited by the carbon substrate, nitrogen substrate, pH or product inhibition. The carbon substrate limitation is first considered. Monod (1949) introduced an empirical description of the relation between the specific rate of biomass growth and limiting substrate concentration $C_S$ as in equation 2.19.

$$\mu_G = \mu_{max} \cdot \frac{C_S}{C_S + K_s} \tag{2.19}$$

The lactic acid product also has an inhibitory effort on the cell growth. Luedeking and Piret (1959) proposed a correction for the effect of the lactic acid concentration and specific growth rate with the constant $\sigma$ as in equation 2.20.

$$\mu_G = \mu_{max} - \sigma \cdot C_P \tag{2.20}$$

Non-competitive product inhibition is expressed in equation 2.21 [35, 36, 37, 38].

$$\mu_G = \mu_{max} \cdot \frac{C_S}{C_S + K_s} \cdot \frac{k_P}{C_P + k_P} \tag{2.21}$$

Where $C_P$ and $C_S$ are the product and substrate concentration. $k_P$ is the product inhibition constant.

There is another formulation of the product inhibition term as shown in equation 2.22 [39, 40].

$$\mu_G = \mu_{max} \cdot \frac{C_S}{C_S + K_s} \cdot (1 - \frac{C_P}{C_{P_{inh}}}) \tag{2.22}$$

Where $C_{P_{inh}}$ is the product concentration above which the microorganism stop growing.

As the formed product is acidic and causes cessation of growth and production, the inhibitory effect of pH has to be included in the model. Fu and Mathews (1999) proposed $\mu_{max}$ and $K_s$ as a function of pH based on a Monod model as in equation 2.23.

$$\mu_G = \mu_{max}(pH) \cdot \frac{C_S}{C_S + K_s(pH)} \tag{2.23}$$

Where

$$\mu_{max}(pH) = 0.523 \cdot exp\left\{-0.16(pH - 5.0)^2\right\} - \frac{0.265}{0.614 + (pH - 4.0)}$$

$$K_s(pH) = 0.605 \cdot exp\left\{0.85(pH - 5.0)^2\right\} + \frac{106.4}{0.65 + (pH - 4.0)}$$

Concerning the product inhibition, it has been noticed that the undissociated form of lactic acid is the main inhibitory component and the influence has to be taken into account apart from the formed product. Schepers, Thibault and Lacroix proposed the specific growth rate as function of carbon substrate, nitrogen substrate, pH, dissociated and undissociated lactic acid concentration as shown in equation 2.24. [42]

$$\mu_G = (\mu_{max} + \beta \cdot pH_c \cdot WP_c)\frac{C_{SC}}{C_{SC} + K_{SC}} \cdot \frac{C_{SN}}{C_{SN} + K_{SN}} \cdot M \cdot N \tag{2.24}$$

where

$$M = \left(\frac{exp(-k_{[HL]}\frac{P}{1+10^{(pH-pKa)}})}{1 + exp(k_{[L^-]}(\frac{P}{1+10^{(pKa-pH)}} - k_{[L^-]}))}\right)$$

$$N = exp\left(\frac{(|pH_{opt} - pH|)_n}{\sigma^2}\right)$$

The term $\beta \cdot pH_c \cdot WP_c$ is the interaction between pH and the whey permeate (WP). The term $\frac{C_{SC}}{C_{SC}+K_s} \cdot \frac{C_{SN}}{C_{SN}+K_{SN}}$ represents the limitation of carbon and nitrogen substrate. The second last term describes the inhibition by undissociated lactic acid and dissociated lactate. The last terms accounts for the pH inhibition.

The lactic acid production rate is described by the model from Luedeking and Piret in equation 2.25. A and B are the coefficients of growth and non-growth associated production.

$$r_p = \frac{dC_P}{Xdt} = A \cdot \mu + B \tag{2.25}$$

Rogers, Bramall and McDonald (1978) included the substrate limitation in the lactic acid production rate as in equation 2.26.

$$r_p = \frac{dC_P}{Xdt} = A \cdot \mu + B\frac{C_S}{C_S + K_s} \tag{2.26}$$

The substrate limitation and product inhibition are described by the kinetic models explained above. For this thesis project, a recent study of *S. thermophiles* LAB kinetic model is referred [4].

### 2.3.3 LAB kinetic model in this study

The kinetic model used for this project is adapted from the work of Aghababaie, Khanahmadi and Beheshti [4]. The work mainly focuses on a complete kinetic model to describe *L. bulgaricus* and *S. thermophiles* growth and lactic acid production rates. This project only considers *S. thermophiles*. The factors of the kinetic model, such as temperature, pH, carbon and nitrogen substrate, dissociated and undissociated lactic acid are analyzed independently. The kinetic model of biomass growth rate is described in the equation 2.27.

$$\frac{dX}{dt} = \mu_{max} f_T f_{pH} f_{SC} f_{SN} f_{La} f_{HLa} X \tag{2.27}$$

Where $f_i$ is one variable fuction that express the impact of factor $i$ on the growth.

Function of temperature ($f_T$):
The Arrhenius law is modified and used to describe the influence of temperature on growth rate in equation 2.28.

$$f_T = \frac{exp(\Delta E_a/RT)}{1 + Aexp(-\Delta G_a/RT)} \tag{2.28}$$

Function of pH ($f_{pH}$):
A four parameter equation is used to describe the pH effect on biomass growth rate, shown in equation 2.29.

$$f_{pH} = \frac{C_1(pH_{opt} - pH)^2 + C_2}{(pH_{opt} - pH)^2 + C_3} \tag{2.29}$$

Function of carbon substrate ($f_{SC}$):
The Monod model is used for the carbon substrate function as in equation 2.30.

$$f_{SC} = \frac{C_{SC}}{C_{SC} + K_{SC}} \tag{2.30}$$

Function of nitrogen substrate ($f_{SN}$):
The nitrogen substrate function is described using Monod as in equation 2.31.

$$f_{SN} = \frac{C_{SN}}{C_{SN} + K_{SN}} \tag{2.31}$$

Function of lactate and lactic acid ($f_{La}$ and $f_{Hla}$) :
The effect of product inhibition is studied for lactate and lactic acid concentrations. From Henderson-Hasselbach correlation, the concentratiron of lactate and lactic acid are calculated from equation 2.32 and 2.33.

$$C_{Hla} = \frac{C_P}{1 + 10^{(pH - pKa)}} \tag{2.32}$$

$$C_{La} = \frac{C_P}{1 + 10^{(pKa - pH)}} \tag{2.33}$$

The exponential function of lactic acid inhabitation effect is obtained from Schepers et al., as in equation 2.34.

$$f_{Hla} = (\frac{1}{1 + e^{K_p(C_{Hla} - K_{Hla})}}) \tag{2.34}$$

The effect of lactate on lactic acid bacteria growth is shown in the equation 2.35.

$$f_{La} = e^{-K_{La}C_{La}} \tag{2.35}$$

Function of lactic acid production rate ($r_p$)
The production rate of lactic acid is obtained from Luedeking-Piret equation shown in equation 2.36.

$$r_p = \frac{dC_p}{dt} = A\frac{dX}{dt} + BX \tag{2.36}$$

Where A is growth associate and B is non-growth associated parameters.

Carbon substrate consumption rate:
From the mass balance, the substrate consumption rate is equal to the sum of product and biomass formation rates [45].

$$\frac{dC_{SC}}{dt} = -1.12\frac{dX}{dt} - 0.95\frac{dC_p}{dt} \tag{2.37}$$

The first term is the conversion rate of biomass and the second terms is the production rate of lactic acid.

Nitrogen substrate consumption rate:
The nitrogen substrate is converted to biomass. The nitrogen consumption rate is shown in equation 2.38.

$$\frac{dC_{SN}}{dt} = -\delta_n\frac{dX}{dt} \tag{2.38}$$

### 2.3.4 CFD model combined with kinetic modelling

Combining the kinetic model with the CFD model will solve the chemical reactions and fluid dynamics in each element in CFD simultaneously. The number of element from CFD can be fine enough to achieve detailed results. pH, substrate and oxygen gradients are obtained by combining CFD and kinetic modelling. However, due to large number of partial differential equations and grids from CFD, the computational demand can be very intensive and sometimes impractical. [44]

There is another approach to avoid the considerable computation time. In this case, the bioreactor domain is divided into a number of compartments. In each compartment, the materials are considered to be well mixed. The solver time can be considerably reduced by the relatively small number of zones compared to the large number of cells from CFD. The compartment model is able to solve for complex biological reactions with a large number of variables in the system. [22]

In this project, the developed model has been developed with the intention to be applied for small size bioreactors and to deliver more accurate results compared to compartment models.

CHAPTER 3

# Materials and methods

The experimental and computational methods used in this project are described in this chapter. A CFD model of a pilot scale bioreactor is set up and validated based on the comparison of mixing time prediction and experimental measurements. Additionally, a kinetic model of the microorganism *S. thermophiles* is implemented into the CFD model. The model was established and solved in commercial software ANSYS CFX 16.1.

## 3.1 Bioreactor geometry

The experiments were carried out in the pilot bioreactor from Danish company Chr. Hansen in Hørsholm. The volume of the bioreactor is about $1m^3$. The pilot bioreactor was built by Chemap AG from Switzerland in the 1980s and the original mechanical drawing of the bioreactor was provided by the company as shown in the appendix A.

The bioreactor consists of a cylindrical tank body with round shape at the bottom. One long impeller shaft is placed in the middle of the tank and the motor is at the bottom. At one side of the bioreactor, an oxygen supply pipe introduces oxygen through the bottom sparger of the bioreactor. The bioreactor inside top view can be seen from the figure 3.1.

Measurements were conducted to define the dimensions of the bioreactor. The bioreactor dimensions used in the CFD model are shown in the figure 3.2 and 3.3.

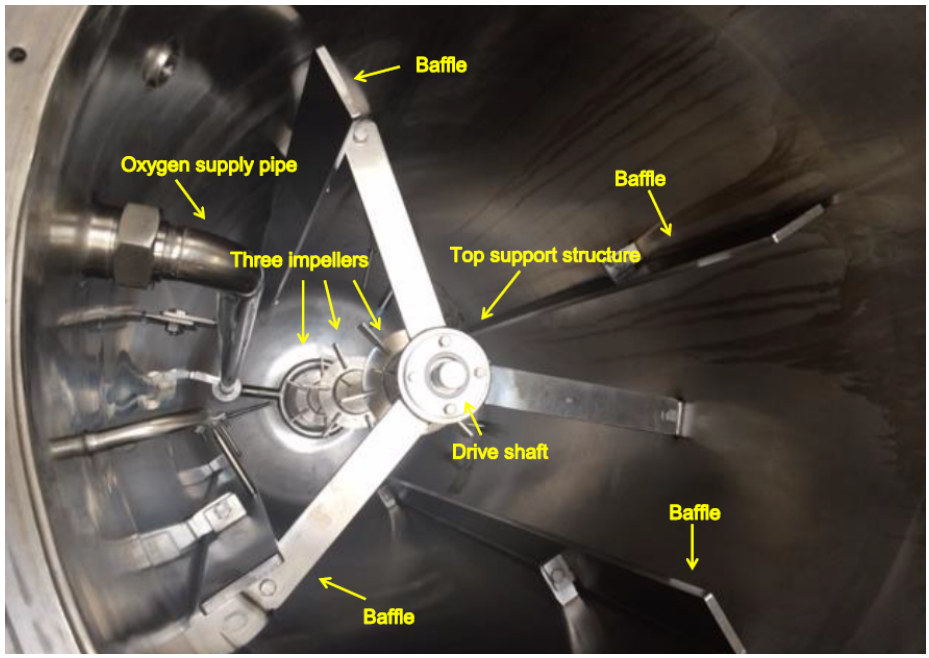


**Figure 3.1:** Bioreactor configuration.

## 3.2 Experimental methods

Mixing time determination experiments were conducted in the pilot bioreactor in Chr. Hansen. Top and bottom pulse mixing time were measured with agitation speed 200rpm and 100rpm. Sensor response time measurements were performed at the DTU lab. The purpose is to study the influence of sensor delay time on the mixing time experiments.

### 3.2.1 Mixing time determination

Mixing time experiments were carried out to measure the mixing time of the bioreactor. As the growth medium is non-viscous and has similar fluid properties as water, tap water is filled in the bioreactor. The filling level is up to $30cm$ from the top. This gives water volume about $750L$ inside the bioreactor. Six pH sensors from Endress+Hauser were used to measure the pH data during the mixing experiments. The pH sensor is type CPS471D which can be fully immersed in water as explained in section 2.2.2. A steel rack as shown in figure 3.4 was built in order to mount the pH sensors.

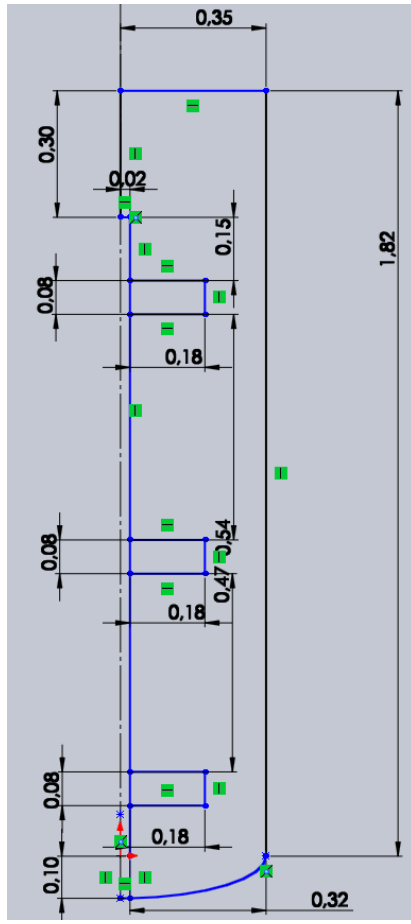


**Figure 3.2:** Tank domain dimensions [m].

The mounted positions of the pH sensors were based on the recirculation loops inside the bioreactor. The recirculation loops are the internal circulation of fluid caused by the impeller agitation. The pH sensors are mounted such that each pH sensor was placed inside one recirculation loop respectively. The height of the sensors from the top can be found in table 3.1.

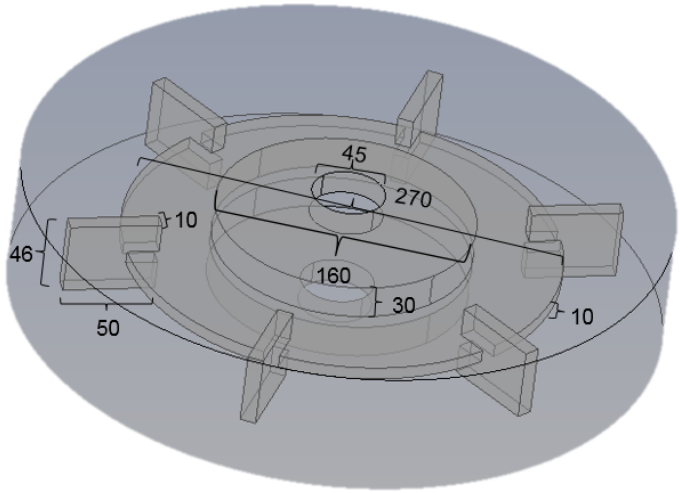


**Figure 3.3:** Impeller domain dimensions [mm].

**Table 3.1:** Height of the pH sensors.

| Sensor no | Distance to the top of the bioreactor (m) |
|---|---|
| 1 | 0.6 |
| 2 | 0.95 |
| 3 | 1.25 |
| 4 | 1.6 |
| 5 | 1.85 |
| 6 | 2.1 |

The mixing time determination experiments were carried out at the agitation speed 200rpm and 100rpm. The experiments were performed with the sodium hydroxide added from the top and bottom of the bioreactor in different experiments. The top dosing position is right in front of the baffle next to the rack. The bottom dosing position is shown in the figure 3.5. pH sensors were calibrated before conducting experiments and pH data were collected and analysed after the mixing time experiments.

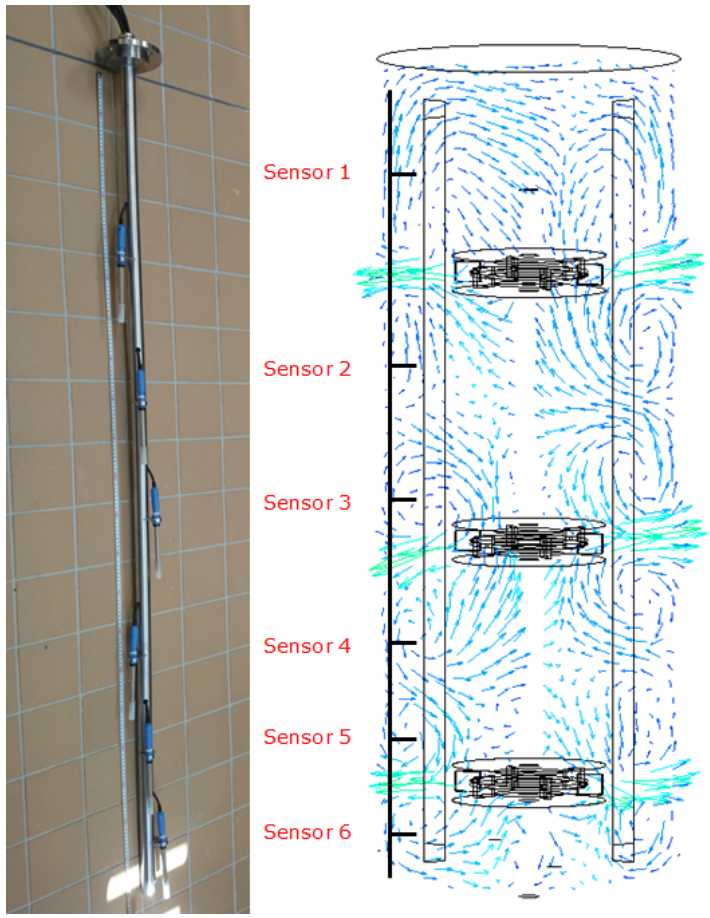


**Figure 3.4:** pH sensors on the rack (left) and recirculation loops from CFD (right).

### 3.2.2 Response time of the pH sensor

pH sensor response time was investigated to see the influence on the mixing time determination. Buffer solutions of pH 4 and 7 were first used. The pH sensor was first immersed in buffer solution at pH 4,then it was removed, washed with tap water and inserted into buffer solution at pH 7. The time for the pH sensor changing to 95% of the final stable pH was calculated. Another experiment switching from buffer solution pH 7 to 4 was performed with the same procedure.

After that, response time of ammonia mixing was determined. a laboratory beaker of 150ml was filled with tap water and stirred by stir bar. pH sensor was first immersed in the water. After the pH measurement was stable, ammonia

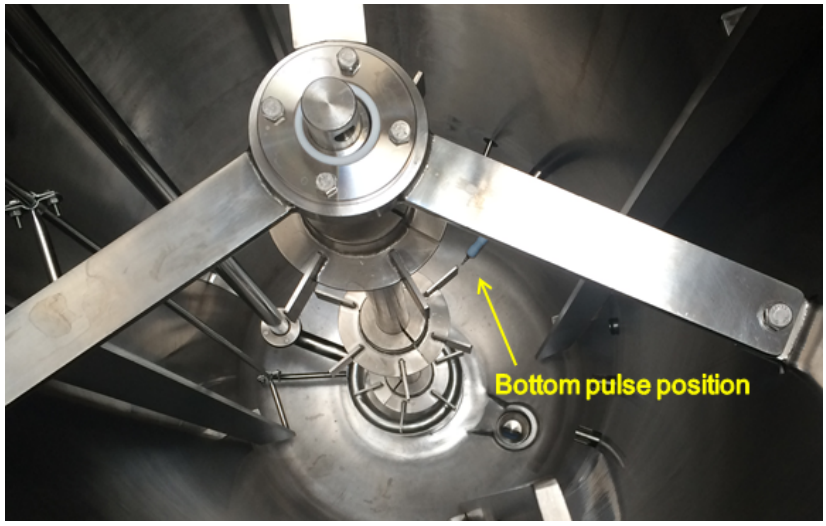


**Figure 3.5:** Bottom pulse dosing position.

solution was added and the time for pH increasing to the final stable value was recorded.

## 3.3 Computational methods

The geometry of the bioreactor was built in SolidWorks 2015. The whole bioreactor is divided into two parts, a tank domain and an impeller domain. The tank domain includes shaft, drive, baffles and cylindrical impeller parts. The impeller domain is cylindrical and includes the detailed geometry of the impeller. The fluid domain defines the region of fluid flow and the domain constrains the region occupied by the fluid by defined walls [18]. The height of the cylindrical tank is 1.8 m which gives domain liquid volume about 750 L.

After the geometry is defined in SolidWorks, it is imported into ICEM-CFD to make meshing. Both unstructured and structured mesh were studied in this project. The comparison of structured and unstructured mesh is shown in figure 3.6.

Before making the structured mesh, the potential of bioreactor geometry simplification is studied in order to see the possibility to neglect the bottom oxygen

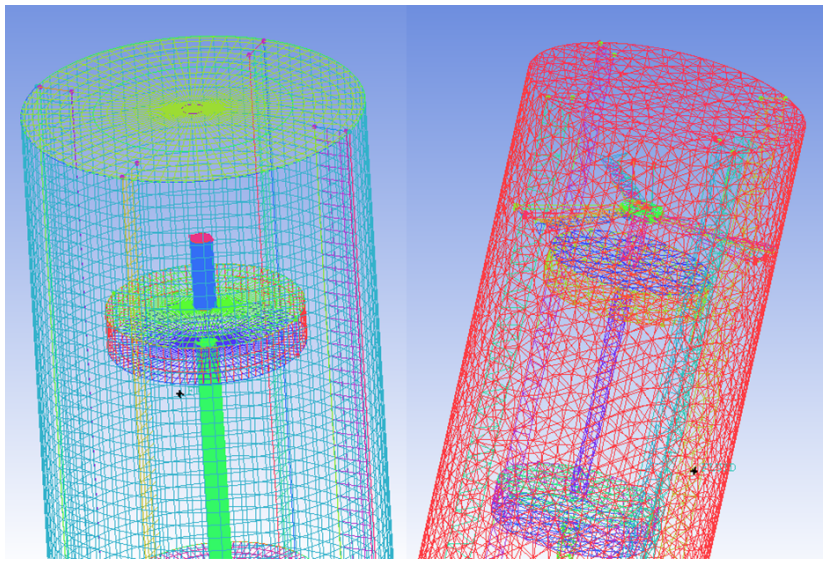

**Figure 3.6:** Structured mesh (left) and unstructured mesh (right) for the tank domain.

sparger and top structure elements. Flow patterns before and after simplification are compared and investigated. Subsequently, a structured mesh without top structure and bottom oxygen sparger is generated.

The flow problem is setup in ANSYS CFX-Pre. First, steady state simulations are carried out. The table 3.2 shows the general CFX-Pre settings for a steady state simulation. The model is shown in the figure 3.7. The simulations are done at the IBM eServer x3455 with two 64-bit AMD Opteron 2218 dual-core CPUs (a total of 648 CPU cores) running at 2.6 GHz.

**Table 3.2:** Steady state CFX-Pre settings.

| **Option** | **Setting** |
|---|---|
| Analysis type | Steady state |
| Tank domain | Material: water |
| | Domain motion: stationary |
| | Buoyancy model: non buoyant |
| | Turbulence option: k-Epsilon |
| | Heat transfer: none |
| Impeller domain | Material: water |
| | Domain motion: rotating |
| | Angular velocity: 200 [rev $min^{-1}$] |
| | Rotation axis: Global Y |
| | Buoyancy model: non buoyant |
| | Turbulence option: k-Epsilon |
| | Heat transfer: none |
| Boundary condition | Tank domain top: free slip wall |
| | Tank domain baffle: no slip wall |
| | Tank domain shaft: rotating wall |
| Advection scheme | High resolution |
| Turbulence model | First order |
| Auto timescale factor | 1.0 |
| Residual type | RMS |
| Residual target | 1.E-4 |
| Interface | Top side of the top impeller |
| | Outer cylinder side of the top impeller |
| | Bottom side of the top impeller |
| | Top side of the middle impeller |
| | Outer cylinder side of the middle impeller |
| | Bottom side of the middle impeller |
| | Top side of the bottom impeller |
| | Outer cylinder side of the bottom impeller |
| | Bottom side of the bottom impeller |

After the flow velocity patterns are available, transient simulation is performed in order to determine the mixing time. The velocity fields from steady state are introduced to the transient simulation. One pulse is added from the top or bottom of the bioreactor based in the experiments. The top pulse is introduced in front of the baffle next to the rack and bottom pulse is injected at the same position and same height as the bottom impeller. Six monitor points are defined at the positions of the pH sensors and pulse concentrations are collected. The

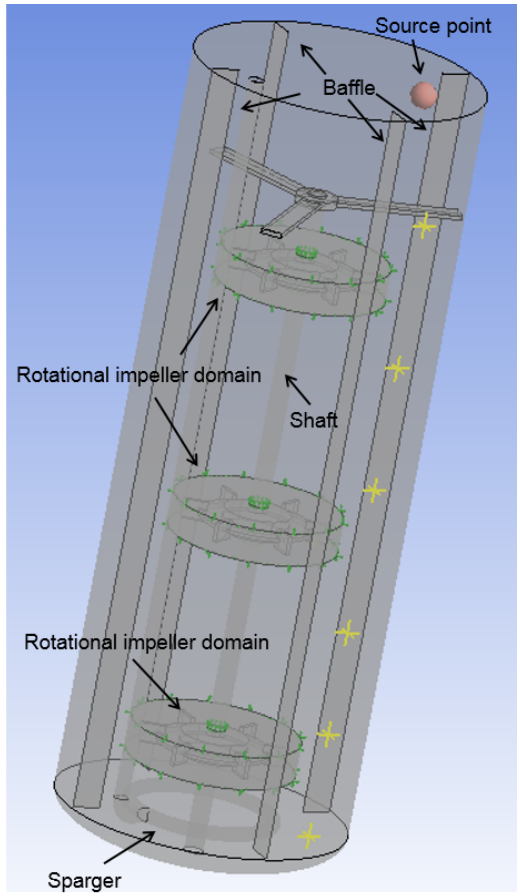


**Figure 3.7:** Model in CFX-Pre.

concentrations are then normalised using equation 2.15 and the mixing time is calculated by equation 2.17 as below.

$$\log \sigma^2 = \log(C_t' - 1)$$

$$\log \sigma_{RMS}^2 = \log \left\{ \frac{1}{n} \sum_{i=1}^{n} (C_{t,i}' - 1)^2 \right\}$$

To obtain the simulated pH, the normalized concentration from CFD is multiplied with the $OH^-$ concentration calculated from the start and final pH values in the pilot experiments. After that, the calculated concentration increment is converted to pH increment and added to the initial pH in the pilot experiments. Figure 3.8

shows how the data from CFD is converted and validated with the help of pilot experiments.

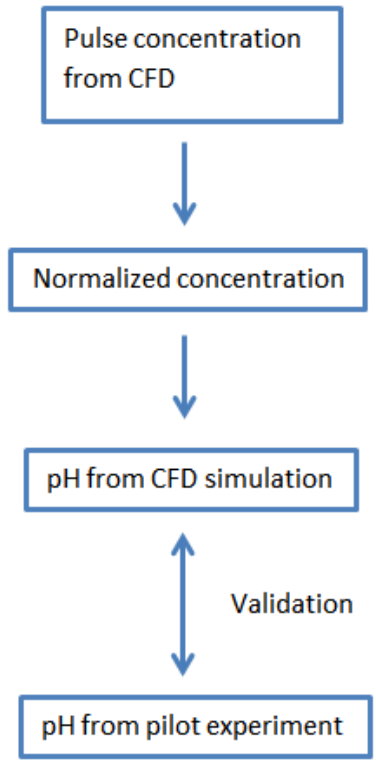


**Figure 3.8:** Validation of CFD simulation with pilot experiment.

## 3.4 Kinetic model

The kinetic model discussed in section 2.3.3 was combined with the CFD model. Agitation speed of 100 rpm and 200 rpm were simulated. The biomass, carbon substrate, nitrogen substrate and product concentrations are defined as additional variables in the CFD model. The function of temperature ($f_T$), function of pH ($f_{pH}$), function of carbon substrate ($f_{SC}$), function of nitrogen substrate ($f_{SN}$), function of lactate ($f_{La}$) and function of lactic acid ($f_{Hla}$) are formulated as expressions from section 2.3.3. The biomass growth rate equation 2.27, lactic acid production rate equation 2.36, carbon and nitrogen substrate consumption rate equation 2.37 and 2.38 are used to describe the kinetics in the bioreactor as below.

$$\frac{dX}{dt} = \mu_{max} f_T f_{pH} f_{SC} f_{SN} f_{La} f_{HLa} X$$

$$\frac{dC_p}{dt} = A\frac{dX}{dt} + BX$$

$$\frac{dC_{SC}}{dt} = -1.12\frac{dX}{dt} - 0.95\frac{dC_p}{dt}$$

$$\frac{dC_{SN}}{dt} = -\delta_n \frac{dX}{dt}$$

The applied constants for the mentioned equations can be found in Aghababaie, Khanahmadi and Beheshti, 2015 [4] and are summarized in the table 3.3. The initial biomass concentration is 0.1g/L. Carbon and nitrogen substrate initial concentration are 20g/L and 10g/L respectively. The initial lactic acid concentration is 0g/L.

**Table 3.3:** Estimated constants for kinetic model.

| Parameter | Value | Unit |
|---|---|---|
| $\mu_{max}$ | 1.18 | 1/h |
| A | 1200000 | - |
| $E_a$ | 130 | kJ/mol |
| $G_a$ | 52160 | kJ/mol |
| $pH_{opt}$ | 6.87 | - |
| $C_1$ | 45.42 | - |
| $C_2$ | 11.25 | - |
| $C_3$ | 0.123 | - |
| $K_c$ | 1.0E-6 | g/L |
| $K_N$ | 253.1 | g/L |
| $K_p$ | 52.862 | L/g |
| $K_{Hla}$ | 0.0444 | g/L |
| $K_{La}$ | 0.3259 | L/g |
| A | 1.54 | g lactic acid/g biomass |
| B | 0.52 | g lactic acid/(g biomass h) |
| $\delta_n$ | 0.98 | g biomass/g nitrogen |

The combined CFD and kinetic model is simulated in the cube reactor without fluid flow, the pilot plant bioreactor with 100rpm and 200rpm as batch operation. The cube reactor is used to compare the results.

# CHAPTER 4

# Results

This chapter describes the simulation results of different CFD model setups, the mixing simulations and the characterization of pH sensors. The validation of pilot experiments and CFD simulations are carried out in section 4.5. The CFD model is integrated with the kinetic model in section 4.6.

## 4.1 CFD simulation

In order to obtain a converged CFD model, the number of elements for several unstructured and structured meshes were studied and different settings of advection scheme and timescale were investigated. pH measurements during pulse experiments are compared with the simulated results.

### 4.1.1 Mesh number study

The study was started with a comparison of the mesh element size. The used mesh was unstructured mesh in the unsimplified tank geometry. Larger mesh elements resulted in poor geometric resolution which could not represent the real geometry. This often happens when there are pipes or fine parts in the fluid domain. The coarse mesh could not capture the fine curves and will result in unreliable simulation results. It can also be seen in the CFX-Pre with unnormal curves. When the mesh element is relatively large, the shape of the local domain is often deformed.

In order to optimize the mesh quality, it is recommend to decrease the size of mesh element smaller or define the pipe or fine part individually using part mesh. Even though fine mesh can define the geometry better, however, more mesh means the computation time increase considerably.

The unstructured mesh study was performed for the full bioreactor geometry. The comparison of the unstructured mesh size is shown in table 4.1. The model of test 1 has about 1.5 million mesh elements in the tank domain. After the part mesh setup was subsequently redefined and the mesh size was reduced, the number of mesh elements increased to about 3 million in test 2. This improved the physical shape of the domain in CFX-Pre. The mesh elements were further increased to about 11 million. This resulted in a long computation time and large steady state files. The large steady state files were used as an input for the transient simulation for each transient step. For this reason, the steady state file should be small enough so the transient simulation doesn't occupy too much memory space.

**Table 4.1:** Unstructured mesh size study.

| Test number | | Test 1 | Test 2 | Test 3 |
|---|---|---|---|---|
| Geometry | | Not simplified | Not simplified | Not simplified |
| Mesh type | | Unstructured mesh | Unstructured mesh | Unstructured mesh |
| Mesh number | Tank elements | 1,558,844 | 2,922,162 | 10,868,395 |
| | Impeller elements | 1,447,855 | 1,447,855 | 1,447,855 |
| Computation time | | NA | 1 day | 2 day 16 hours |
| Convergence | | Unconverged | Converged | Converged |

### 4.1.2 Advection scheme and timescale study

The settings of advection schemes with high resolution, upwind, specified blend factor and timescale factors are studied in this section. The mesh for this study was done with an unstructured mesh for the unsimplified tank geometry.

The purpose is to investigate advection schemes of high resolution, upwind, specified factor and timescale setting to get converged results. Table 4.2 shown the simulations of the advection scheme specified blend factor varying from 0.3 to 0.9. Unfortunately, the results are not converged. Table 4.3 shows the studies of upwind advection scheme and timescale from 0.1 to 1 with the step of 0.1. From timescale factor 0.1 to 0.4, the simulations were not converged. Table 4.4 shows that the converged results were obtained at timescale factor from 0.5 to 1. The

last two test simulated at the high resolution which didn't converge and different monitor points achieving same converged result with advection schemes upwind.

**Table 4.2:** Unstructured mesh specified blend factor study.

| **Test number** | | **Test 1** | **Test 2** | **Test 3** | **Test 4** |
|---|---|---|---|---|---|
| Geometry | | Not simplified | Not simplified | Not simplified | Not simplified |
| Mesh type | | Unstructured mesh | Unstructured mesh | Unstructured mesh | Unstructured mesh |
| Mesh number | Tank elements | 2,922,162 | 2,922,162 | 1,944,154 | 2,922,162 |
| | Impeller elements | 1,447,855 | 1,447,855 | 2,061,695 | 1,447,855 |
| Computation time | | NA | NA | NA | NA |
| Convergence | | Unconverged | Unconverged | Unconverged | Unconverged |
| Remark | | Specified blend factor 0.3 | Specified blend factor 0.6 | Specified blend factor 0.75 | Specified blend factor 0.9 |

### 4.1.3 Simplification of the geometry

It was investigated whether the bioreactor geometry could be simplified without loosing too much quality of the CFD model. As seen in figure 3.1, the bioreactor geometry of the top support structure and the oxygen sparger are complicated. It can be time-consuming in order to make such geometry for structured mesh. Therefore, the influence of the top support and oxygen pipe structure on the

**Table 4.3:** Upwind advection scheme and timescale study 0.1 to 0.4.

| **Test number** | | **Test 1** | **Test 2** | **Test 3** | **Test 4** |
|---|---|---|---|---|---|
| Geometry | | Not simplified | Not simplified | Not simplified | Not simplified |
| Mesh type | | Unstructured mesh | Unstructured mesh | Unstructured mesh | Unstructured mesh |
| Mesh number | Tank elements | 1,944,154 | 1,944,154 | 1,944,154 | 1,944,154 |
| | Impeller elements | 2,061,695 | 2,061,695 | 2,061,695 | 2,061,695 |
| Computation time | | NA | NA | NA | NA |
| Convergence | | Unconverged | Unconverged | Unconverged | Unconverged |
| Remark | | Upwind auto factor 0.1 | Upwind auto factor 0.2 | Upwind auto factor 0.3 | Upwind auto factor 0.4 |

**Table 4.4:** Upwind advection scheme and timescale study 0.5 to 1.

| **Test number** | | **Test 1** | **Test 2** | **Test 3** | **Test 4** |
|---|---|---|---|---|---|
| Geometry | | Not simplified | Not simplified | Not simplified | Not simplified |
| Mesh type | | Unstructured mesh | Unstructured mesh | Unstructured mesh | Unstructured mesh |
| Mesh number | Tank elements | 1,944,154 | 1,944,154 | 1,944,154 | 1,944,154 |
| | Impeller elements | 2,061,695 | 2,061,695 | 2,061,695 | 2,061,695 |
| Computation time | | 2 days | 1 day 17 hours | 2 days 3 hours | 1 day 4 hours |
| Convergence | | **Converged** | **Converged** | **Converged** | **Converged** |
| Remark | | Upwind auto factor 0.5 | Upwind auto factor 0.6 | Upwind auto factor 0.7 | Upwind auto factor 0.8 |
| **Test number** | | **Test 5** | **Test 6** | **Test 7** | **Test 8** |
| Geometry | | Not simplified | Not simplified | Not simplified | Not simplified |
| Mesh type | | Unstructured mesh | Unstructured mesh | Unstructured mesh | Unstructured mesh |
| Mesh number | Tank elements | 1,944,154 | 1,944,154 | 1,944,154 | 1,944,154 |
| | Impeller elements | 2,061,695 | 2,061,695 | 2,061,695 | 2,061,695 |
| Computation time | | 2 days | 1 day 3 hours | 1 day 6 hours | NA |
| Convergence | | **Converged** | **Converged** | **Converged** | Unconverged |
| Remark | | Upwind auto factor 0.9 | Upwind auto factor 1 | Different monitor points | High resolution |

fluid flow pattern was investigated first. Such structures behave as walls for the neighbouring fluid. However, in terms of fluid bulk flow, the influence is quite limited. Figure 4.1 and 4.2 show the top views which are taken 50 mm above the top support structure and the oxygen pipe.

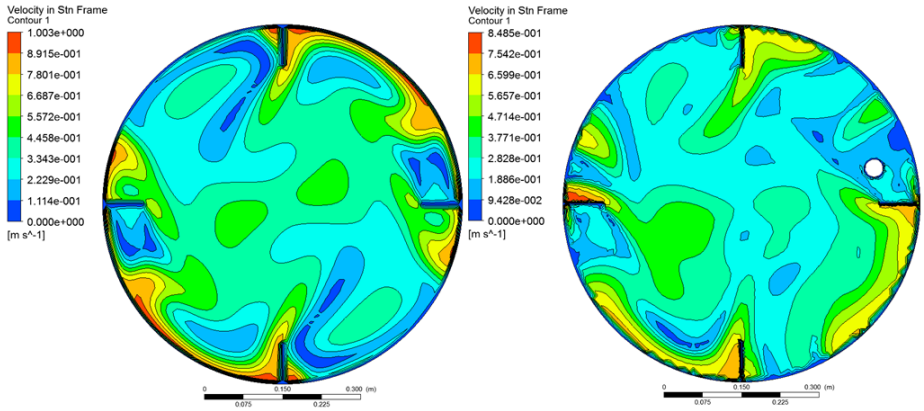


**Figure 4.1:** The influence of top support structure for simplified (left) and unsimplified (right) geometry.

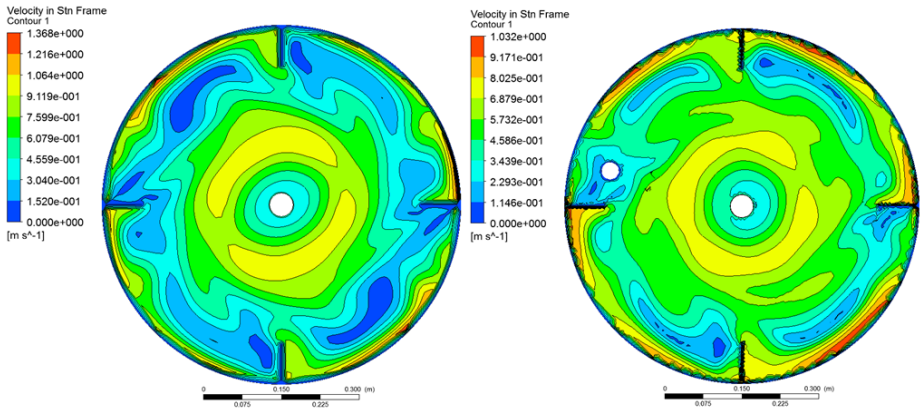


**Figure 4.2:** The influence of bottom oxygen pipe for simplified (left) and unsimplified (right) geometry.

At the neighbour areas, the velocity is zero and the flow is cut due to the wall effect. But the flow above and below such structures are not much influenced. This can also see from figure 4.3. The velocity profile and the flow circulation loops are not influenced by the complex structures and the same circulation loops can be observed. As a consequence, the top and bottom structure was simplified and neglected for further structured mesh studies.

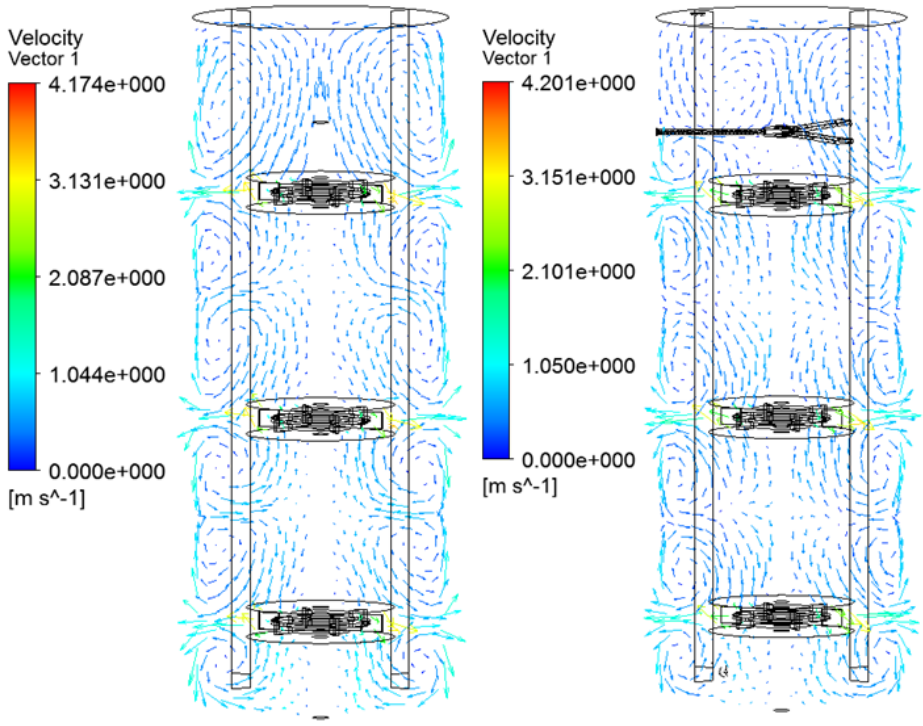


**Figure 4.3:** Velocity vector comparision for simplified (left) and unsimplified (right) geometry .

### 4.1.4 Structured mesh study

The structured mesh convergence results are shown in table 4.5. Converged simulations can be obtained from advection scheme with high resolution as well as with upwind and specified factors. Furthermore, the time to achieve convergence is less compared to unstructured mesh.

Test 4 is used to structured and unstructured simulation results. The computation time for the structured mesh model is 19 hours with advection scheme upwind auto factor 1 while it took more than one day for the unstructured mesh model to get converged. The predicted fluid circulation loops of both simulations are quite similar. Figure 4.3 shows the equal velocity vectors from the side view. Six circulation loops can be observed from each side. Two loops are created by each impeller on the top and bottom side. The velocity contours at the top impeller are compared in the figure 4.4 and 4.5. The flow in front of the impeller blades are forced out and flow behind the impeller fill in. This creates turbulence

**Table 4.5:** Structured mesh study.

| **Test number** | | **Test 1** | **Test 2** | **Test 3** | **Test 4** |
|---|---|---|---|---|---|
| Geometry | | Simplified | Simplified | Simplified | Not simplified |
| Mesh type | | Structured mesh | Structured mesh | Structured mesh | Unstructured mesh |
| Mesh number | Tank elements | 1,539,356 | 1,539,356 | 1,539,356 | 1,944,154 |
| | Impeller elements | 1,509,526 | 1,509,526 | 1,509,526 | 2,061,695 |
| Computation time | | 16 hours | 23 hours | 19 hours | 1 day 3 hours |
| Convergence | | Converged | Converged | Converged | Converged |
| Remark | | High resolution | Specified factor 0.75 | Upwind auto factor 1 | Upwind auto factor 1 |

around the impeller and improves mixing. The flow velocity around the baffle is reduced and multi-mixing zones are created.

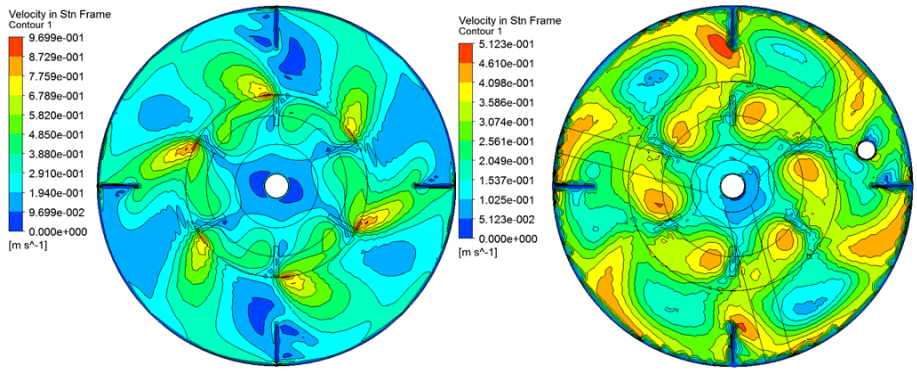


**Figure 4.4:** Top view velocity profile comparsion structured (left) and unstructured (right) mesh upwind.

Structured mesh tests were conducted for different tank and impeller element numbers. The purpose is to find the proper mesh size. Above such mesh size, finer mesh does not improve the simulation results. The number of tank mesh elements varied from 500k to 100k and impeller mesh element from 500k to 200k as shown in table 4.6. It can be seen that test 1 (tank domain 982,008 and impeller domain 508,744 mesh element) and test 7 (tank domain 112,596 and

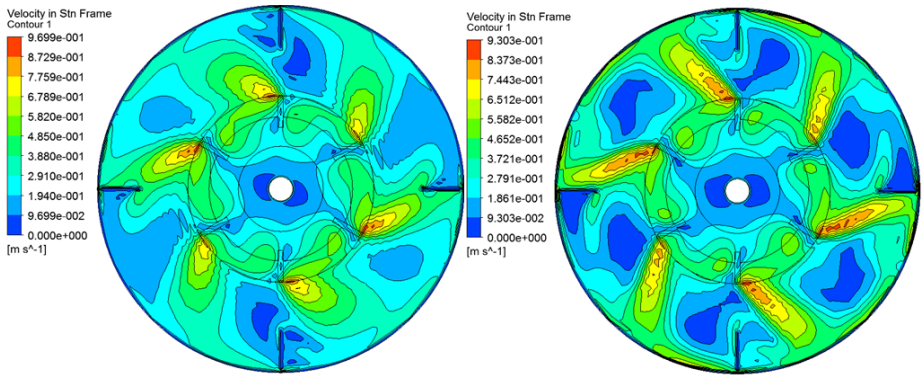


**Figure 4.5:** Top view velocity profile comparsion structured mesh upwind (left) and high resolution (right).

impeller domain 508,744 mesh element) are converged. The convergence depends on the node correlation on the interface of tank and impeller domains. Test 7 has only half of the mesh elements compared with Test 1. Mixing time predictions of both models are compared in the section 4.5.

**Table 4.6:** Structured mesh element study.

| **Test number** | | **Test 1** | **Test 2** | **Test 3** | **Test 4** |
|---|---|---|---|---|---|
| Geometry | | Simplified | Simplified | Simplified | Simplified |
| Mesh type | | Structured mesh | Structured mesh | Structured mesh | Structured mesh |
| Mesh number | Tank elements | 982,008 | 982,008 | 492,192 | 492,192 |
| | Impeller elements | 508,744 | 199,880 | 508,744 | 199,880 |
| Convergence | | **Converged** | Unconverged | Unconverged | Unconverged |
| **Test number** | | **Test 5** | **Test 6** | **Test 7** | **Test 8** |
| Geometry | | Simplified | Simplified | Simplified | Simplified |
| Mesh type | | Structured mesh | Structured mesh | Structured mesh | Structured mesh |
| Mesh number | Tank elements | 246,960 | 246,960 | 112,596 | 112,596 |
| | Impeller elements | 508,744 | 199,880 | 508,744 | 199,880 |
| Convergence | | Unconverged | Unconverged | **Converged** | Unconverged |

## 4.2 Sensor response time determination

The sensor response time was measured in the lab for the pH sensor. It was observed that the pH sensor started to change the pH reading immediately after placing it into the buffer solution or adding ammonia in the beaker. It took around 4s for the sensor to reach 95% of the final pH value, see table 4.7.

The normalized concentration and log $\sigma_2$ RMS plot of one of the ammonia mixing experiment is shown in figure 4.6 and 4.7.

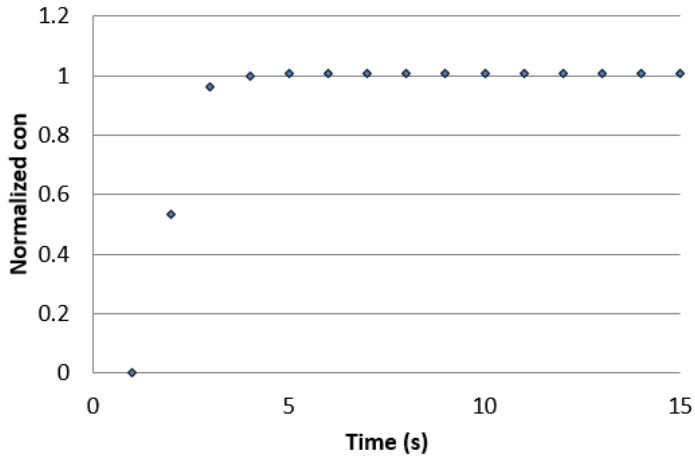


**Figure 4.6:** Response time normalized concentration.

## 4.3 Pilot mixing time experiments

Mixing time experiments were carried out in the pilot-scale bioreactor. The results obtained are shown in table 4.8. The experimental concentration is normalised with the help of equation 2.15 as below.

**Table 4.7:** Response time measurement.

| Test | Response time (s) |
|---|---|
| pH 4 to 7 | 5 |
| pH 7 to 4 | 3 |
| Ammonia | 3 |
| Ammonia | 3 |

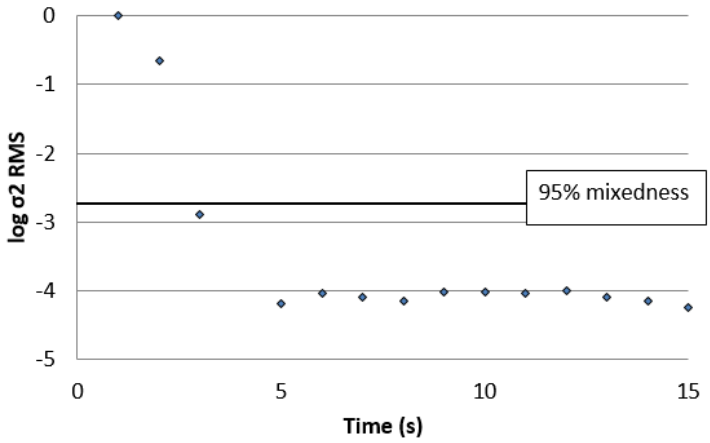


**Figure 4.7:** Response time log $\sigma_2$ RMS.

$$C_i' = \frac{C_i - C_0}{C_\infty - C_0}$$

Mixing time is calculated from equation 2.17 as below.

$$\log \sigma_{RMS}^2 = \log \left\{ \frac{1}{n} \sum_{i=1}^{n} (C_{t,i}' - 1)^2 \right\}$$

In experiment 1, the impeller speed was set to be 200rpm and sodium hydroxide was added from the top. Sensor 1 did not work properly and it was omitted from the evaluation. Experiment 2 and 3 were performed at the impeller speed 200rpm and NaOH was added from the same top position but with different amount. For experiment 4, the tracer pulse was added from bottom of the bioreactor as shown in figure 3.5. The impeller speed was set to be 200rpm. For experiment 5, the impeller speed was set to be 100rpm and sodium hydroxide was added from the top position. Unfortunately, sensor 5 was not working in experiment 5 and had to be omitted from the evaluation.

**Table 4.8:** Pilot mixing time experiments.

| Experiment No. | Impeller speed (rpm) | NaOH dosing position | $OH^-$amount ($10^{-3}$mol) | Mixing time (s) |
|---|---|---|---|---|
| **1** | 200 | Top | 0.2 | 60 |
| **2** | 200 | Top | 5 | 84 |
| **3** | 200 | Top | 1.7 | 113 |
| **4** | 200 | Bottom | 1.7 | 67 |
| **5** | 100 | Top | 4 | 267 |

Despite the sodium hydroxide dosing position, it can be seen that mixing time is around 60 to 110 seconds at impeller speed 200rpm. When reducing impeller speed to 100rpm, the mixing time increases significantly to 267s due to less turbulence in the bioreactor like in the pilot experiment.

The normalised concentration and log $\sigma^2$ RMS of experiment 1 is shown in figure 4.8 and 4.9. In the normalized plot, the normalized concentrations of each sensor start from 0 and goes to 1 in the end. Sensor 2 and 3 overshoot and the remaining sensors increase gradually. The log $\sigma^2$ RMS decreases rapidly from 0 to -2.5 and reaches -2.6 at 60s. The normalized concentration and log sigma RMS of the rest experiments can be found in appendix C.

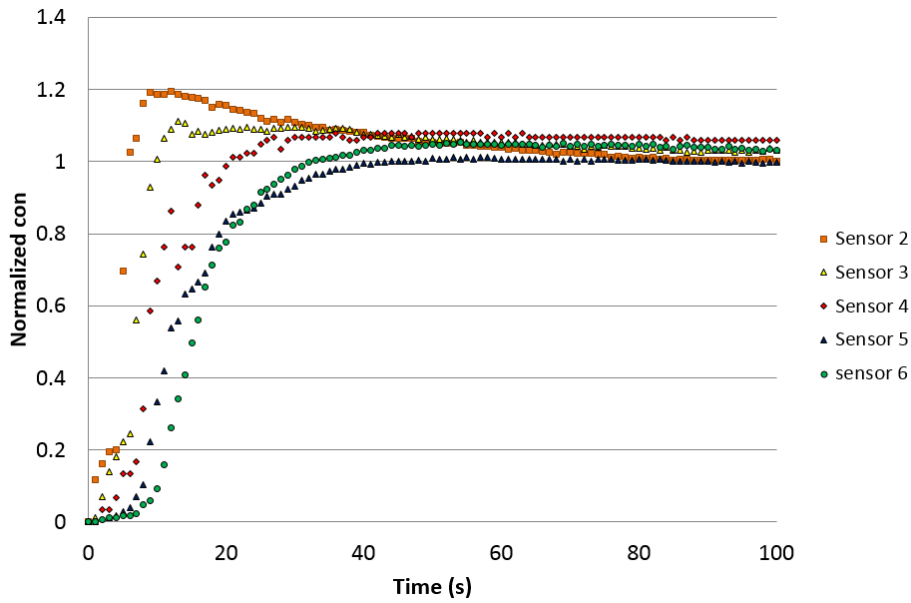


**Figure 4.8:** Normalized concentration of pilot mixing experiment 1.

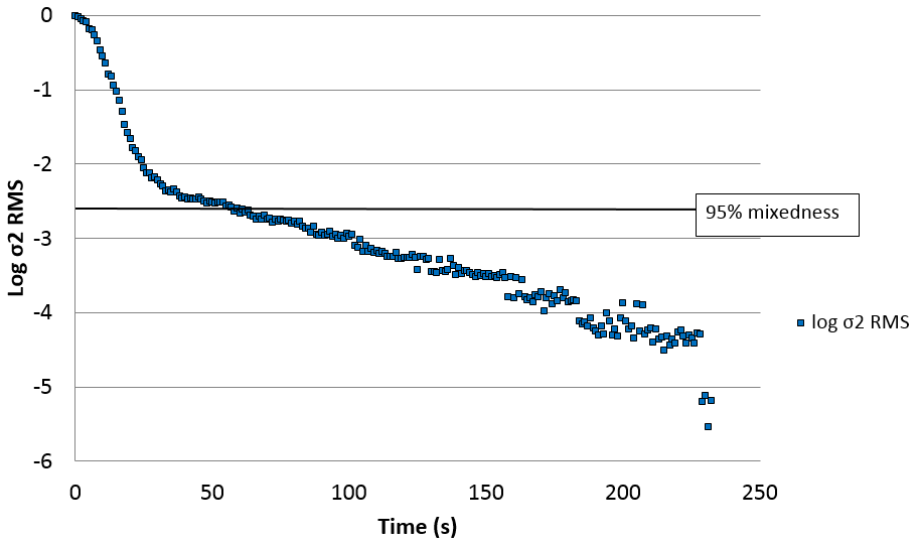


**Figure 4.9:** Mixing time of pilot mixing experiment 1.

Reynolds number of impeller speed 200rpm and 100rpm were calculated from the equation 2.14. The Reynolds number are 443260 for 200rpm and 221603 for 100rpm respectively.

## 4.4 CFD mixing time simulations

The CFD mixing time simulations are summarised in table 4.9. The tracer pulse is set to be source point added from the top or bottom of the bioreactor. Simulation 1, 3 and 4 have the same number of mesh elements. Different amount of pulse were added for the transient simulations but the mixing time is the same. The simulation of structured mesh 1 achieves 76s mixing time and simulation 2 yields 90s with only half of the mesh elements. The model with reduced mesh elements requires less computational power and reduce the accuracy at the same time. For the unstructured mesh, the mixing time is only 50s to achieve homogeneity. Simulation 6 is carried out by injecting the pulse from the bottom and it results in 86s mixing time counting from adding the pulse. Simulation 7 with impeller speed 100rpm achieves 152s mixing time.

**Table 4.9:** CFD mixing time simulations.

| CFD simulation number | Mesh type | Mesh element | | Pulse specification | Impeller speed (rpm) | Mixing time (s) |
|---|---|---|---|---|---|---|
| | | Tank elements | Impeller elements | | | |
| 1 | Structured mesh | 982,008 | 508,744 | 1kg pulse for 1s | 200 | 76 |
| 2 | Structured mesh | 122,596 | 508,744 | 1kg pulse for 1s | 200 | 90 |
| 3 | Structured mesh | 982,008 | 508,744 | 5kg pulse for 1s | 200 | 76 |
| 4 | Structured mesh | 982,008 | 508,744 | 0.01kg pulse for 1s | 200 | 76 |
| 5 | Unstructured mesh | 2,795,653 | 529,744 | 1kg pulse for 1s | 200 | 50 |
| 6 | Structured mesh | 982,008 | 508,744 | 0.1kg pulse for 10s from bottom | 200 | 86 |
| 7 | Structured mesh | 982,008 | 508,744 | 1kg pulse for 1s | 100 | 152 |

Tracer concentration gradients are observed when adding the pulse to the bioreactor. Figure 4.10 shows the tracer gradients at time 1s, 5s, 20s and 40s with a top pulse at 200rpm impeller speed. The tracer gradient of 200rpm with a bottom pulse and 100rpm with a top pulse are shown in the appendix B.

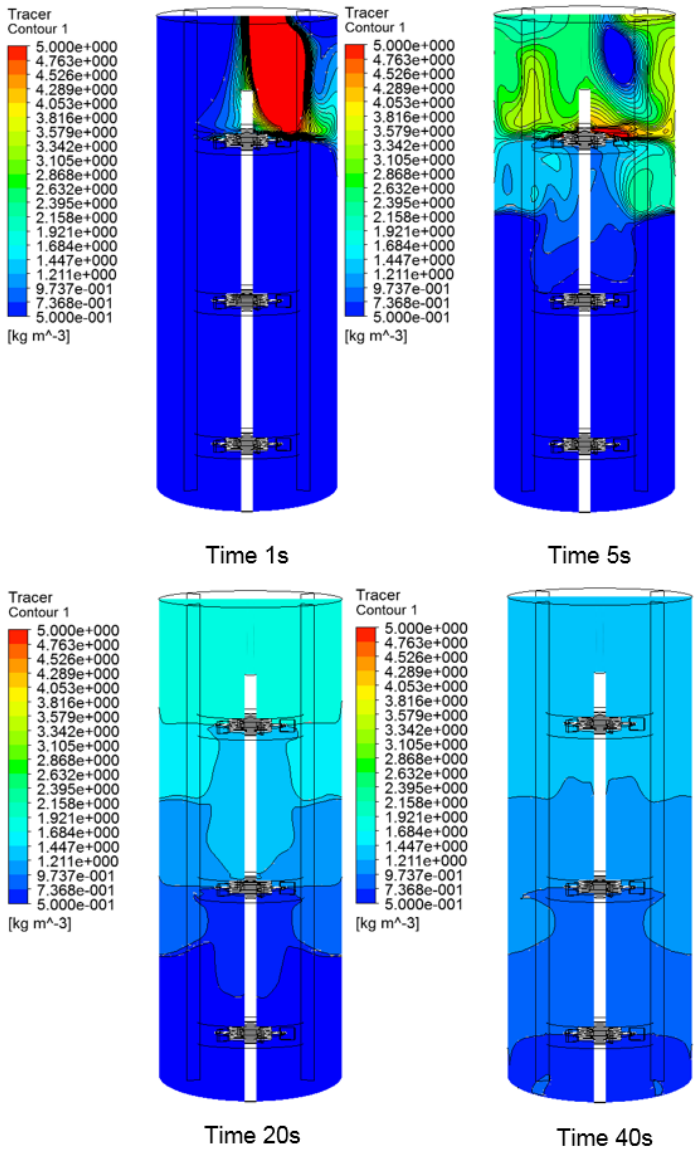


**Figure 4.10:** Tracer gradient at 200rpm and top polse.

## 4.5 Comparison of CFD mixing time simulations with the experimental results

The concentration data obtained from CFD simulations are converted to pH values and compared with the pilot mixing experiments.

Experiment 1:

The experimental and CFD simulated pH values are shown in figure 4.11. The experiment was carried out with 200rpm impeller speed and sodium hydroxide added from the top of bioreactor. Sensor 2 overshoots at around first 10 seconds and then the pH value decreases and reaches the final pH. For the bottom sensor 6, it takes almost the same time (about 6s) before the sensor started to change value in both the pilot experiment and CFD simulations. The simulated pH trajectories capture the experimental dynamics very well. The mixing time is predicted similar as 60s and 76s for pilot experiment and CFD simulation respectively.

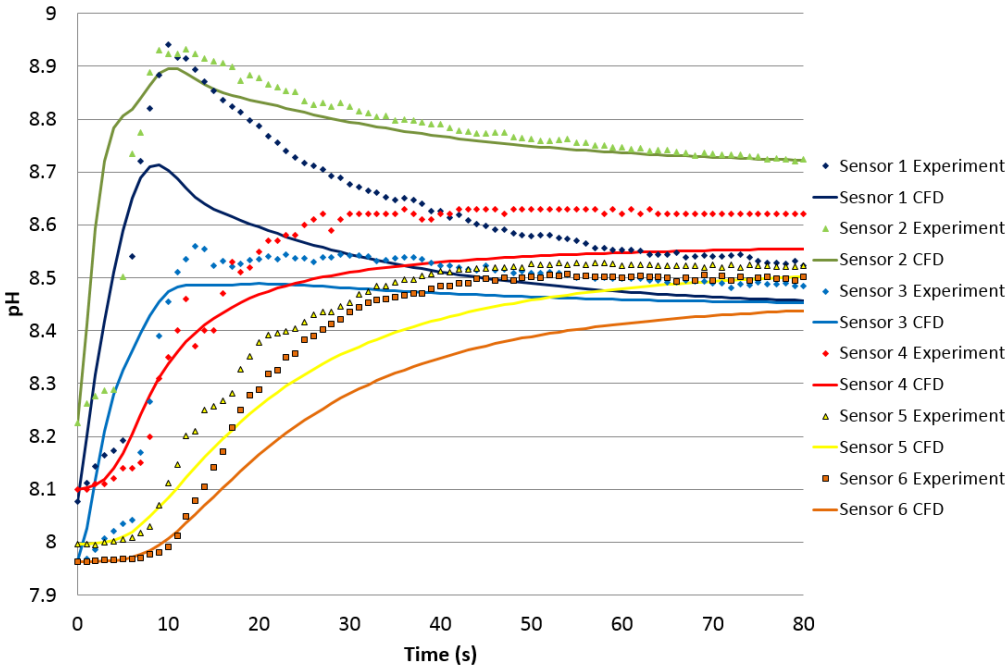


**Figure 4.11:** Experiment 1 (200rpm, top pulse).

Experiment 2:

The experimental and CFD simulated pH data is shown in figure 4.12. The experiment was performed at 200rpm impeller speed and sodium hydroxide added from the top of the bioreactor. Sensor 1, 2, 3 overshoot and then decrease to steady values while for sensor 4, 5, 6 the pH increase gradually. The pH increments for all the sensor are predicted well by CFD simulation. During the pilot experiment, sensor 1, 2 and 3 have a lag time about 6s before the sensor started to change pH values. The mixing time from the pilot experiment is 84s and 76s for the CFD simulation.

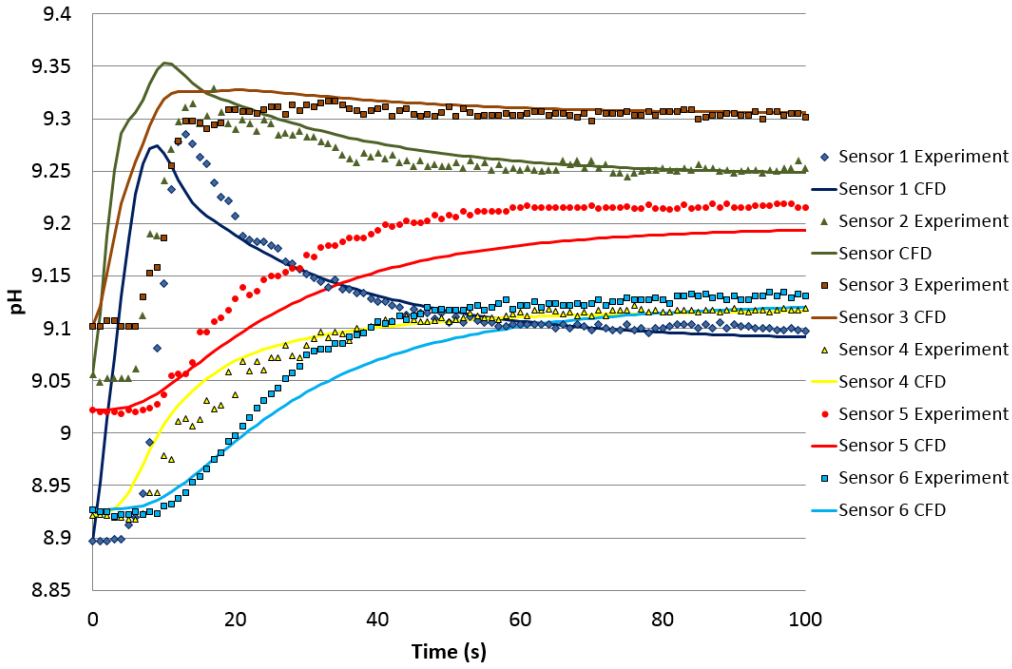


**Figure 4.12:** Experiment 2 (200rpm, top pulse).

Experiment 3:

The experimental and CFD simulated pH data is shown in figure 4.12. The experiment was performed at 200rpm impeller speed. The amount of sodium hydroxide added from the top of the bioreactor is about $0.2 \cdot 10^{-3}$ mol. Generally the CFD simulated pH values are lower compared with the experimental data. The CFD simulation determined 76s mixing time while pilot experiment needed 113s to reach 95% mixedness.

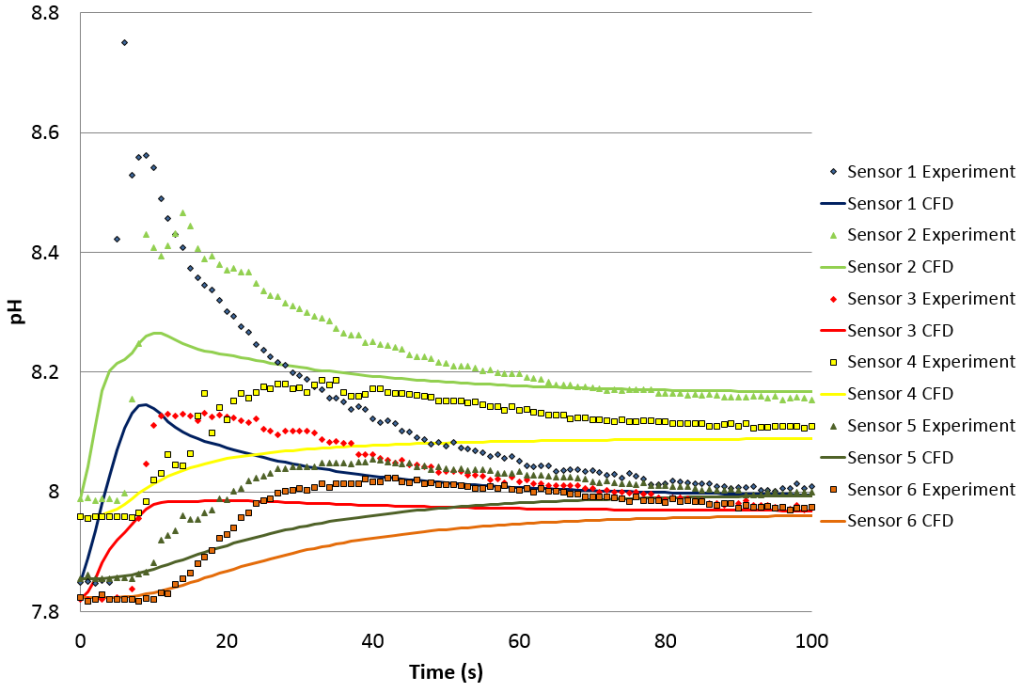


**Figure 4.13:** Experiment 3 (200rpm, top pulse).

Experiment 4:

Experiment 4 was conducted by adding sodium hydroxide from the bottom of the bioreactor at 200rpm impeller speed. The NaOH is delivered by the hose and the starting time is difficult to determine. Figure 4.14 shows the result after matching the pilot experiment starting time with the CFD simulation time. Sensor 5 and 6 start from pH 8 and reach a peak of pH 9.4 after the pulse is injected. Subsequently, pH values decrease gradually and stabilize around 9 in the end. Similar predictions can be observed from the other sensors. The CFD simulation predicts the pH increment and dynamics very well. The mixing time for pilot and CFD experiment is 67s and 86s respectively.

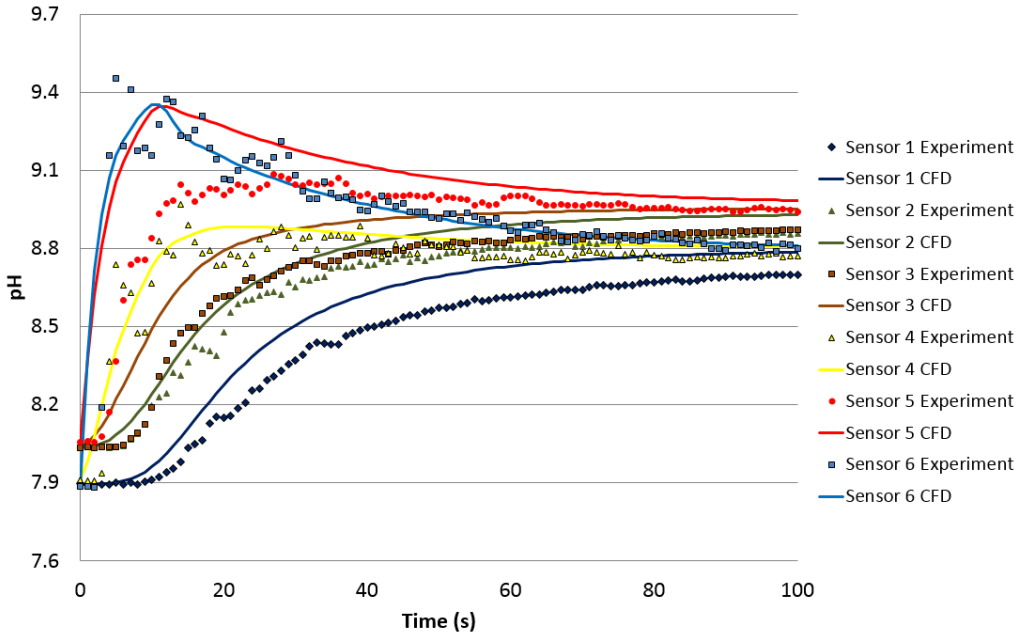


**Figure 4.14:** Experiment 4 (200rpm, bottom pulse).

Experiment 5:

Experiment 5 is done at impeller speed 100rpm. A mixing time of 267 s is achieved. Sensor 1 starts from pH 8.78 and increases to 9.1 after 15s. In the following, it goes down slowly and reaches a stable pH value. The CFD simulation of sensor 1 (dark blue line) predicts the behaviour and dynamics same as in the pilot experiment. Similar behaviours of the other simulated data and experimental figures can be observed. As for the CFD simulation, the mixing time is 152s.

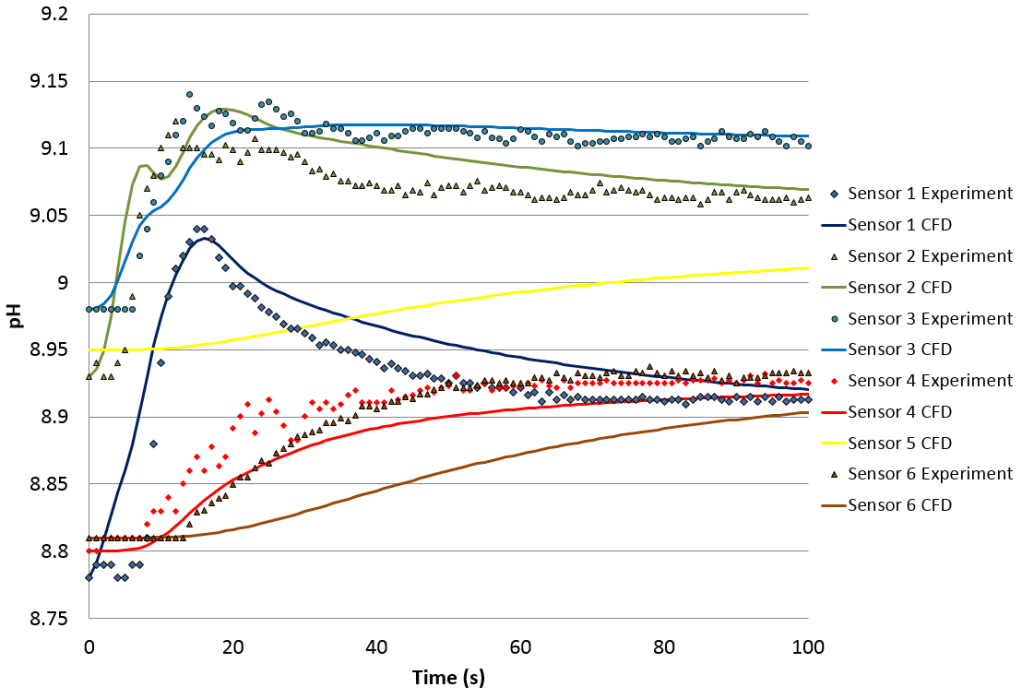


**Figure 4.15:** Experiment 5 (100rpm, top pulse).

The comparison of pilot experiments and CFD simulations is summarised in table 4.10.

The tables 4.11 compares the calculated mixing time of 85% mixedenss with mixing time at similar impeller speed from literature [30].

**Table 4.10:** Comparison of pilot and CFD experiments.

| Impeller speed (rpm) | NaOH dosing position | $OH^-$ amount ($10^{-3}$mol) | Pilot experiment mixing time (s) | CFD simulated mixing time (s) |
|---|---|---|---|---|
| 200 | Top | 1.7 | 60 | 76 |
| 200 | Top | 4 | 84 | 76 |
| 200 | Top | 0.2 | 113 | 76 |
| 200 | Bottom | 5 | 67 | 86 |
| 100 | Top | 1.7 | 267 | 152 |

## 4.6 Kinetic model

Simulations with combined CFD and kinetic equations were performed. One ideal reactor geometry without flow, one bioreactor with 100rpm steady state velocity profile and one bioreactor with 200rpm steady state velocity profile in batch operation were simulated and the resulting growth and consumption diagrams can be seen in the figure D.1, D.2 and D.3.

It can be seen that after about 6 hours, the carbon substrate concentration is consumed and becomes zero. The product concentration grows gradually and stops after the carbon substrate is depleted. Nitrogen substrate and biomass concentrations reach to stable values of 6g/L and 4.2g/L after 6 hours cultivation. With the increasing of product concentration, the growth rate of biomass and consumption rates of carbon and nitrogen substrates are inhibited.

When combining the three kinetic diagrams together, it can be seen that 100rpm and 200rpm show the same curve while there is slight difference in cube reactor.

Generally, the CFD model with structured mesh after optimization predicts the mixing time and pH dynamics very well. The kinetic model works fine when combined with the CFD model.

**Table 4.11:** Mixing time comparison of pilot experiments with literature.

| **Reactor** | **Working volume (L)** | **Impeller type** | **Agitation speed ($s^{-1}$)** | **Mixing time 85% (s)** | **Source** |
|---|---|---|---|---|---|
| Bioreactor 500L | 350 | Two Rushton turbines | 1.66 | 24 | Delvigne 2006 |
| Bioreactor 500L | 350 | Two Rushton turbines | 3.33 | 20 | Delvigne 2006 |
| Bioreactor 1000L | 750 | Three Rushton turbines | 1.66 | 44 | This study |
| Bioreactor 1000L | 750 | Three Rushton turbines | 3.33 | 20 | This study |
| Bioreactor 1000L | 750 | Three Rushton turbines | 3.33 | 32 | This study |
| Bioreactor 1000L | 750 | Three Rushton turbines | 3.33 | 74 | This study |
| Bioreactor 1000L | 750 | Three Rushton turbines | 3.33 | 39 | This study |
| Bioreactor 2000L | 1200 | Two Rushton turbines | 1.81 | 26 | Delvigne 2006 |
| Bioreactor 2000L | 1200 | Two Rushton turbines | 2.36 | 26 | Delvigne 2006 |
| Bioreactor 2000L | 1800 | Three Rushton turbines | 1.81 | 52 | Delvigne 2006 |
| Bioreactor 2000L | 1800 | Three Rushton turbines | 2.36 | 53 | Delvigne 2006 |

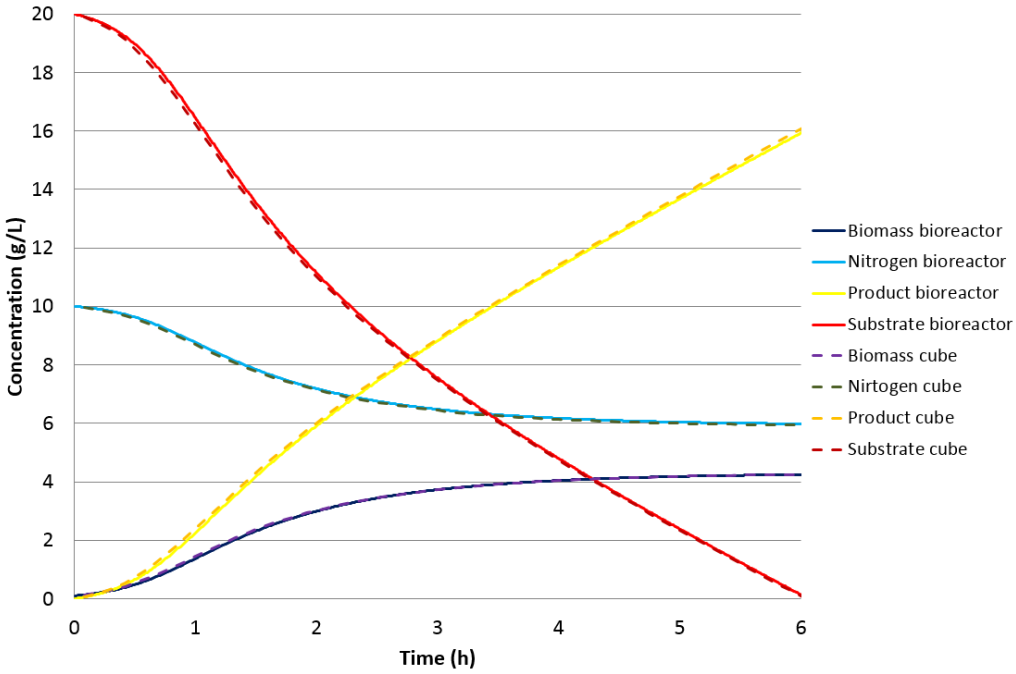


**Figure 4.16:** Combined kinetic curves of a cube reactor and bioreactor at 200rpm and 100rpm batch operation.

# CHAPTER 5

# Discussions

This section discusses the advantage of using a structured mesh, CFD model in predicting the pilot-scale mixing experiments.

The use of a structured mesh results in a reliable CFD model for describing the fluid dynamic conditions of a pilot-scale bioreactor. The mixing time prediction from the structured mesh is more accurate than the unstructured mesh CFD model. In terms of the mesh elements, the structured mesh elements use less elements than the unstructured mesh. However, it is time consuming to fabricate a structured mesh. On the other hand, less mesh elements mean less computational time for the simulation. For complex geometries, it would be difficult to make such model. The unstructured mesh, on the other hand, can be very convenient despite the consequences that the computational power demand is higher.

Geometry simplification can be carried out when the simplified parts are not essential. The bulk flow changes are negligible when omitting the oxygen sparger and top structure. But in terms of producing a structured mesh, the simplified geometry is easier and less time consuming. It is always beneficial to check the possibility for geometry simplification for a structured model as well as for an unstructured model. The resulting flow patterns are not influenced but the time and efforts for a simulation can be reduced.

The influence of the rack with the pH sensors is negligible as seen from the geometry simplification. The bulk flow for the whole bioreactor is not influenced by the rack geometry. The fluid flow simulated with the help of the CFD model has similar radial and axial flow patterns compared with literature [2]. The recirculation loops are formed above and below the impeller. Seen from the top view, the dead zones and turbulence regions around the baffles behave expected.

The CFD model based on the structured mesh predicts the mixing time and pH dynamics very well. In terms of prediction accuracy, the structured mesh model can achieve better and more reliable results than unstructured mesh. This is due to the nodes correlations in the structured mesh. Such correlations are easier for computer to achieve accurate results

In terms of mixing time prediction, the structured mesh CFD model achieves precise and reliable results. As shown in table 4.9, the CFD model based on the unstructured mesh results in shorter mixing time (50s) compared with the pilot experiment. Both structured meshes (simulation 1 and 2) predict the mixing time in the experimental range. The finer the mesh, the better the prediction. The structured mesh is time-consuming to fabricate but it gives better simulation results.

In pilot experiment 3, peaks are visible at sensor 1 and 2. But in CFD simulation, those peaks cannot be observed in simulated pH data. This can be caused by the small amount of sodium hydroxide. In the CFD simulation 4, sensor 5 behaves similar to sensor 6. A possible explanation is that the exact injection position is located between sensor 5 and 6 but it is difficult to measure.

Sensor number 6 is located almost at the bottom of the bioreactor. The fluid flow at this area could be critical due to the wall influence. This might be the reason why sensor 6 pH value from CFD simulations is always lower than that from pilot experiments.

The Reynolds number in the 200rpm and 100rpm miixng cases are 443206 and 221603 respectively. Turbulence is generated inside the recirculation loops and the $k$-$\epsilon$ model is predicting the fluid behaviour well. The mixing in the circulation loops is efficient but it takes time for the tracer to transfer between the loops. However, the equation 2.14 calculates the Reynolds number with one impeller while there are three in the bioreactor and the realistic Reynolds number is higher than calculated.

The pH sensor responses time is approximately 4s. Compared to the mixing time which is 60s to 113s at 200rpm and 267s at 100rpm. The response time

is very small compared to the overall mixing time. The sensor response time influence is negligible.

The CFD model predicts mixing time as well the mixing dynamic behaviour in the system. The pH overshooting and increment are predicted as in the pilot experiments. As shown in figure 4.11 to 4.15, the CFD model not only predicts the slope and final value of the mixing time but also describes the overshooting and increasing dynamics of each sensor

During the mixing experiments, the mixing time is about 60s to 113s at 200rpm impeller speed and 267s at 100rpm impeller speed. Longer mixing time at lower impeller is expected as in the literature [30]. CFD mixing simulations also show that there are tracer gradients even after 40s mixing time. The top and bottom pulse simulations ended up with similar gradients. The 100rpm simulation ended up to longer mixing time. This means pH gradients are generated every time ammonia is added for pH control.

The mixing time varies from 60s to 113s at 200rpm. One of the reasons could be variations from the system that causes the time range. It can be seen from the log $\sigma^2$ RMS figures C.2, C.4 and C.8 in Appendix C, the log $\sigma^2$ RMS is fluctuating around 95% mixedness. It is difficult to define the proper mixing time due to data fluctuations. In pilot experiment 3, the sodium hydroxide adding amount influences the prediction of simulated pH data, see figure 4.13. The $OH^-$ adding amount is one of the reasons that the mixing time varies.

As shown in the table 4.11, the mixing from this study is between 20s to 74s at 200rpm and 44s at 100rpm (85% mixedness). The literature [30] has similar mixing time range.

The combined kinetic and CFD model shows similar growth and consumption kinetics of cube, 200rpm and 100rpm simulations. This is due to there is no initial concentration gradients in the bioreactor. However, combined kinetic and CFD model can predict the local concentrations at any specific locations. The difference of cube reactor and bioreactor in table 4.16 is due to the calculations in the mesh. Cube reactor represents one mesh element and bioreactor has more

than 2.5 million mesh cell which give calculation deviations. However, the difference is very small which proofs the CFD model is accurate.

pH gradients can be expected during the LAB fermentation process. The top pulse experiments is regarded as the fed of substrate from the top. It causes concentration gradients of substrate, growth rate and product. The most critical part is the bottom pulse which is regarded as the pH control during the LAB fermentation process. pH gradient in appendix B is created every time pH control adds ammonia into the process frequently. Such pH gradient causes growth and consumption rate gradients and further substrate and product gradients. The process efficiency and productivity can be influenced significantly.

CHAPTER 6

# Conclusion and future work

A good mixing time prediction of CFD model is achieved compared to the pilot experiments. Despite that, the detailed concentration change at each time step is also well predicted. In terms of prediction accuracy, structured mesh model can achieve better and more reliable results than unstructured mesh.

During the mixing experiments, the mixing time is between 60s to 113s at 200rpm impeller speed and 267s at 100rpm impeller speed. The long mixing time can also be observed in the tracer gradients simulated with the CFD model.

Combined CFD and kinetic model predicts the product growth and substrate consumptions as expected for the fermentation experiments. Combined kinetic and CFD model can predict the concentrations locally. Compared to the simulation from Matlab or compartment model, the information provided from kinetic and CFD model is abundant and powerful.

The CFD model based on the structured mesh results in good mesh quality and accurate simulation results. It is recommended to use the structured mesh to build CFD models although it is time-consuming.

Geometry simplification can help to omit not relevant geometry parts which are not influencing the bulk flow considerably. The simplified geometry makes it easier to create structured mesh. The comparison of bulk flow before and after the geometry simplification is necessary. The parts not influencing the bulk flow can then be omitted.

The future work is to simulate the fed-batch and pH control operations to create concentration or pH gradients in the bioreactor. The flow pattern changes the substrate concentrations and the different growth rate and inhibition rate are created. In this way, the gradients of substrate, product and pH in the bioreactor are simulated. The gradients can be then visualized with CFX-Post and the dynamic gradient change has great interest for cell growth inhibition.

The transient substrate concentration, product or pH gradients can be compared with experiments to validate the accuracy of the combined CFD and kinetic model. Scale-down experiments are suggested after the gradients in the bioreactor are obtained.

The ideal experimental setup would be using conductivity sensors and buffered systems for stabilizing the pH. In that way, the concentrations in the system are obtained directly and pH deviations are avoided.

# Bibliography


[1] Versteeg, H., Malalasekera, W. (1995).
An introduction to computational fluid dynamics The finite volume method. New York: Longman Scientific Technical.

[2] Chapter 6 Mixing
*https://webcache.googleusercontent.com/search?q=cache:2MvOTV_y5nIJ:*
*https://www.researchgate.net/file.PostFileLoader.*
Date: 30/05/2016, Time 11:42 AM.

[3] Bird, R., Stewart, W., Lightfoot, E. (1960).
Transport Phenomena. New York: John Wiley Sons.

[4] Aghababaie, M., Khanahmadi, M., Beheshti, M. (2015).
Developing a detailed kinetic model for the production of yogurt starter bacteria in single strain cultures. Food Bioproducts Processing 94, 657-667.

[5] Kuipers, J., van Swaaij, W. (1998).
Computational Fluid Dynamics Applied to Chemical Reaction Engineering. Advances in Chemical Engineering 24, 227-319.

[6] Anderson, J. (1995).
Computational Fluid Dynamics: The Basics with Applications. New York: McGrawhill Inc.

[7] Shaw, T. (1988).
Predicting Vehicle Aerodynamics Using Computational Fluid Dynamics - A User's Perspective Research in Automotive Aerodynamics. SAE Special Publication 747, 119.

[8] Middleton, J., Pierce, F., Lynch, P. (1986).
Computations of Flow Fields and Complex Reaction Yield in Turbulent Stirred Reactors, and Comparison With Experimental Data. Chemical Engineering Research Design, 18-88.

[9] Delafosse, A. (2014).
CFD-based Compartment Model for Description of Mixing in Bioreactors. Chemical Engineering Science 106, 76-85.

[10] Enfors, S. (2001).
Physiological Responses to Mixing in Large Scale Bioreactors. J. Biotechnol 85, 175-185.

[11] Scott-Pomerantz, C. (2004).
The k-epsilon Model in the Theory of Turbulence. PhD Thesis: University of Pittsburgh.

[12] Srinophakun, T., Jitjaroenchai, J. (2000).
Computational Fluid Dynamics for Predicting Mixing Behavior in kacker's Yeast Fermenter. PhD Thesis: Kasetsart University and King Mongkut's University of Technology Thonburi.

[13] Moilanen, P., Laakkonen, M., Aittamaa, J. (2005).
Modelling Fermenters with CFD. European Symposium on Computer Aided Process Engineering 15.

[14] Delafosse, A., Collignon, M., Calvo, S., Delvigne, F., Crine, M., Thonart, P., et al. (2014).
CFD-based Compartment Model for Description of Mixing in Bioreactors. Chemical Engineering Science 106, 76-85.

[15] ANSYS® Academic Research. (2013).
ANSYS CFX Reference Guide. Release 15.0, ANSYS, Inc.

[16] ANSYS® Academic Research. (2013).
ANSYS CFX-Solver Manager User's Guide. Release 15.0, ANSYS, Inc.

[17] ANSYS® Academic Research. (2013).
Help System, CFX Introduction, Release 15.0. ANSYS, Inc.

[18] ANSYS® Academic Research. (2013).
ANSYS CFX-Solver Theory Guide. Release 15.0, ANSYS, Inc.

[19] Gregory, B. (2011).
Bioreactor Design for Chemical Engineers. American Institute of Chemical Engineers, 21-26.

[20] Jagani, H., Hebbar, K., Gang, S., Raj, P., Chandrashekhar, R., Rao, J. (2010).
An Overview of Fermentation and the Design Considerations to Enhance Its Productivity. Pharmacologyonline 1, 261-301.

[21] Enfors, S. (2001).
Fermentation Process Engineering. Stockholm: Royal Institute of Technology.

[22] Villadsen, J., Nielsen, J., Lidén, G. (2011).
Bioreaction Engineering Principles. New York: Springer.

[23] Rault, A., Bouix, M., Beal, C. (2009).
Fermentation pH Infulence the Physiologicaal-State Dynamics of Lactobacillus bulgaricus CFL1 during pH-Controlled Culture. Applied and Environmental Microbiology, P. 4374 - 4381.

[24] Ascanio, G. (2015).
Mixing time in stirred vessels: A review of experimental techniques. Chinese Journal of Chemical Engineering 23 1065–1076

[25] pH and conductivity
*http://www.unigraphinternational.com/en/pdf_infotech/pH_and_conductivity.pdf.*
Date: 01/06/2016, Time 10:35 AM.

[26] Conductivity theory and practise
*http://www.analytical-chemistry.uoc.gr/files/items/6/618/agwgimometria_2.pdf*
Date: 01/06/2016, Time 11:05 AM.

[27] Conductivity Sensor 4019
*http://www.aanderaa.com/media/pdfs/Conductivity-Sensor-4019.pdf.*
Date: 01/06/2016, Time 17:05 PM.

[28] Endress+Hauser.
Technical Information Tophit CPS471 and CPS471D.

[29] Paul, E., Atiemo-Obeng, V., Kresta, S. (2004).
Handbook of industrial mixing. John Wiley Sons, Inc.

[30] Delvigne, F., Destain, J., Thonart, P. (2006).
A methodology for the design of scale-down bioreactors by the use of mixing anf circulation stochastic models. Biochemical Engineering Journal 28, 256-268.

[31] Halasz, A. (2009).
Lactic Acid Bacteria. Food quality and standards, Vol. III.

[32] Sharpe, M. (1979).
Lactic Acid Bacteria in the Diary Industry. Journey of the Society of Diary Technology, Vol. 32, No.1.

[33] Resat, H., Petzold, L., Pettigrew, M. (2009).
Kinetic Modelling of Biological Systems. Computational systems biology, vol. 541.

[34] Luedeking, R., Piret, E. (1959).
Transient and steady states in continuous fermentation: Theory and experiments. J. Biochem. Microbiol. Technol. Eng. 1 , 431–459.

[35] Powell, G. (1984).
Growth kinetics of non-competitive product inhibition in batch cultures. J. Chem. Tech. Biotechnol. 34, 33–38.

[36] Ohara, H., Hiyama, K., Yoshida, T. (1992).
Non-competitive product inhibition in lactic acid fermentation from glucose. Appl. Microbiol. Biotechnol. 36, 773–776.

[37] Cachon, R., Diviès, C. (1993).
Modeling of growth and lactate fermentation by Lactococcus lactis

subsp. lactis biovar. Diacetylactis in batch culture. Appl. Microbiol. Biotechnol. 40, 28–33.

[38] Pinelli, D., González-Vara, A., Matteuzzi, D., Magelli, F. (1997). Assessment of kinetic models for the production of L- and D-lactic acid isomers by Lactobacillus casei DMS 20011 and Lactobacillus coryniformis DMS 20004 in continuous fermentation. J. Ferment. Bioeng. 83, 209–212.

[39] Keller, A., Gerhardt, P. (1975). Continuous lactic acid fermentation of whey to produce a ruminant feed supplement high in crude protein. Biotechnol. Bioeng. 17, 997–1018.

[40] Monteagudo, J., Rodriguez, L., Rincón, J., Fuertes, J. (1997). Kinetics of lactic acid fermentation by Lactobacillus delbrueckii on beet molasses. J. Chem. Tech. Biotechnol. 68, 271–276.

[41] Fu, W., Mathews, A. (1999). Lactic acid production from lactose by Lactobacillus plantarum: Kinetic model and effects of pH, substrate and oxygen. Biochem. Eng. J. 3, 163–170.

[42] Schepers, A., Thibault, J., Lacroix, C. (2002) Lactobacillus helveticus growth and lactic acid production during pH-controlled batch cultures in whey permeate/yeast extract medium. Part I: Multiple factor kinetic analysis. Enzyme Microb. Technol. 30, 176–186.

[43] Rogers, P., Bramall, L., McDonald, I. (1978) Kinetic analysis of batch and continuous culture of Streptococcus cremoris HP1. Can. J. Microbiol. 24, 372–380.

[44] Babajimopoulos, A., Assanis, D., flowers, D., Aceves, S., Hessel, R. (2005). A fully coupled computational fluid dynamics and multi-zone medel with detailed chemical kinetics for the simulation of premixied charge compression ignition engines. Special issue paper, 497.

[45] Venkatesh, K., Okos, M., Wankat, P. (1993).
Kinetic Model of Growth and Lactic Acid Production from Lactose by Lactobacillus bulgaricus. Process Biochemistry 28, 231-241.

[46] Gadgil, C., Venkatatesh, K. (1997).
Structured Model for Batch Culture Growth of Lactobacillus bulgaricus. J. Chem. Tech. Biotechnol. 68, 89-93.

[47] Monod, J. (1949).
The Growth of Bacterial Cultures. Annual Review of Microbiology.

[48] Schepers, A., Thibault, J., Lacroix, C. (2002).
Lactobacillushelveticus growth and lactic acid production duringpH-controlled batch cultures in whey permeate/yeast extractmedium. Part II: Kinetic modeling and model validation. Enzyme Microb. Technol, 30 (2), 187–194.

[49] ANSYS® Academic Research. (2013).
ANSYS CFX-Solver Modeling Guide. Release 15.0, ANSYS, Inc.

APPENDIX A

# Bioreactor mechanical drawing

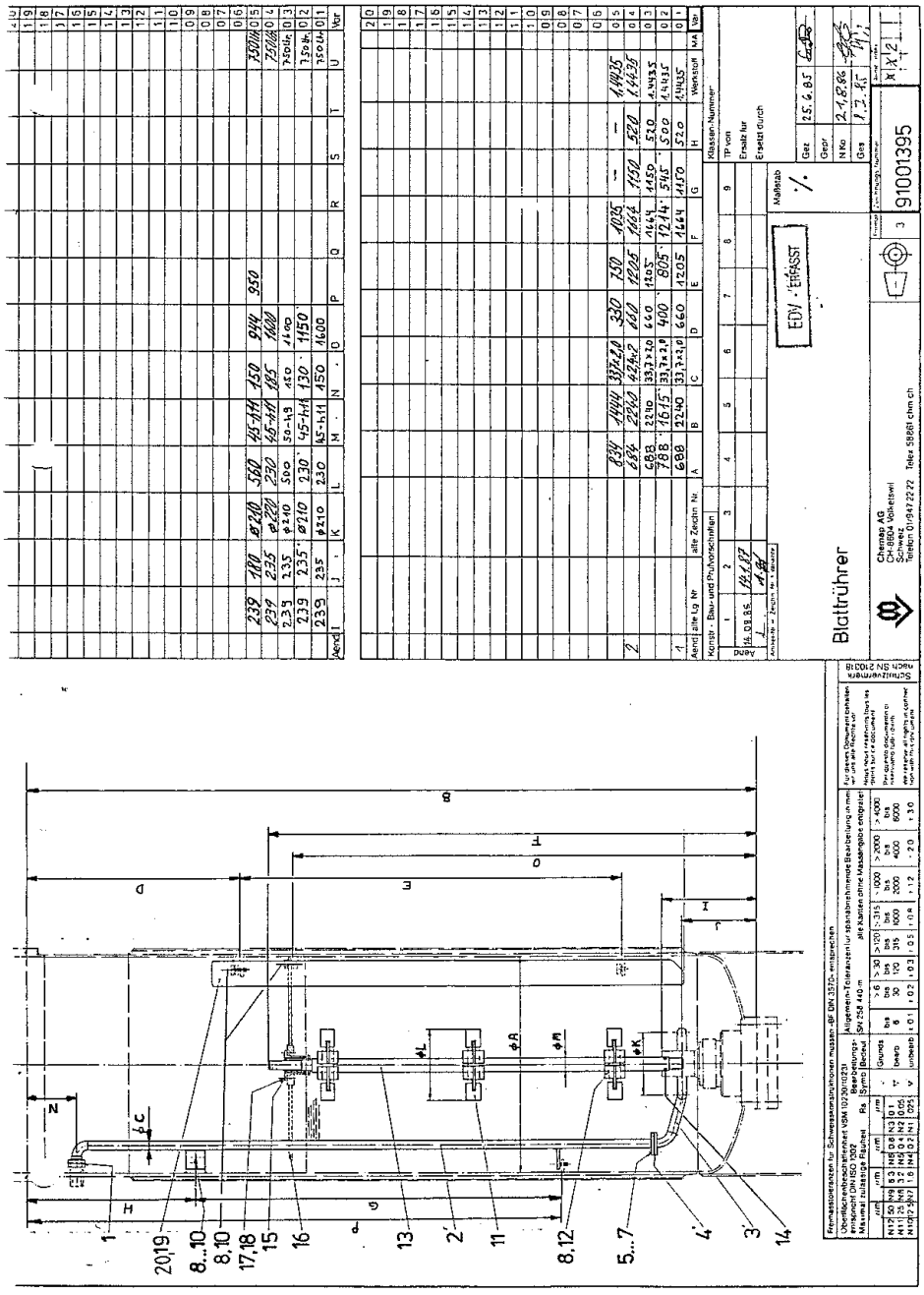
Blattführer
Chemap AG
CH-8340 Hinwil
Schweiz
Telefon 01/947 22 22
Telex 58681 chm ch
EDV - erfasst
91001395
Schutzvermerk nach SN 21021 B

APPENDIX B

# Tracer gradients of bottom pulse and 100rpm top pulse

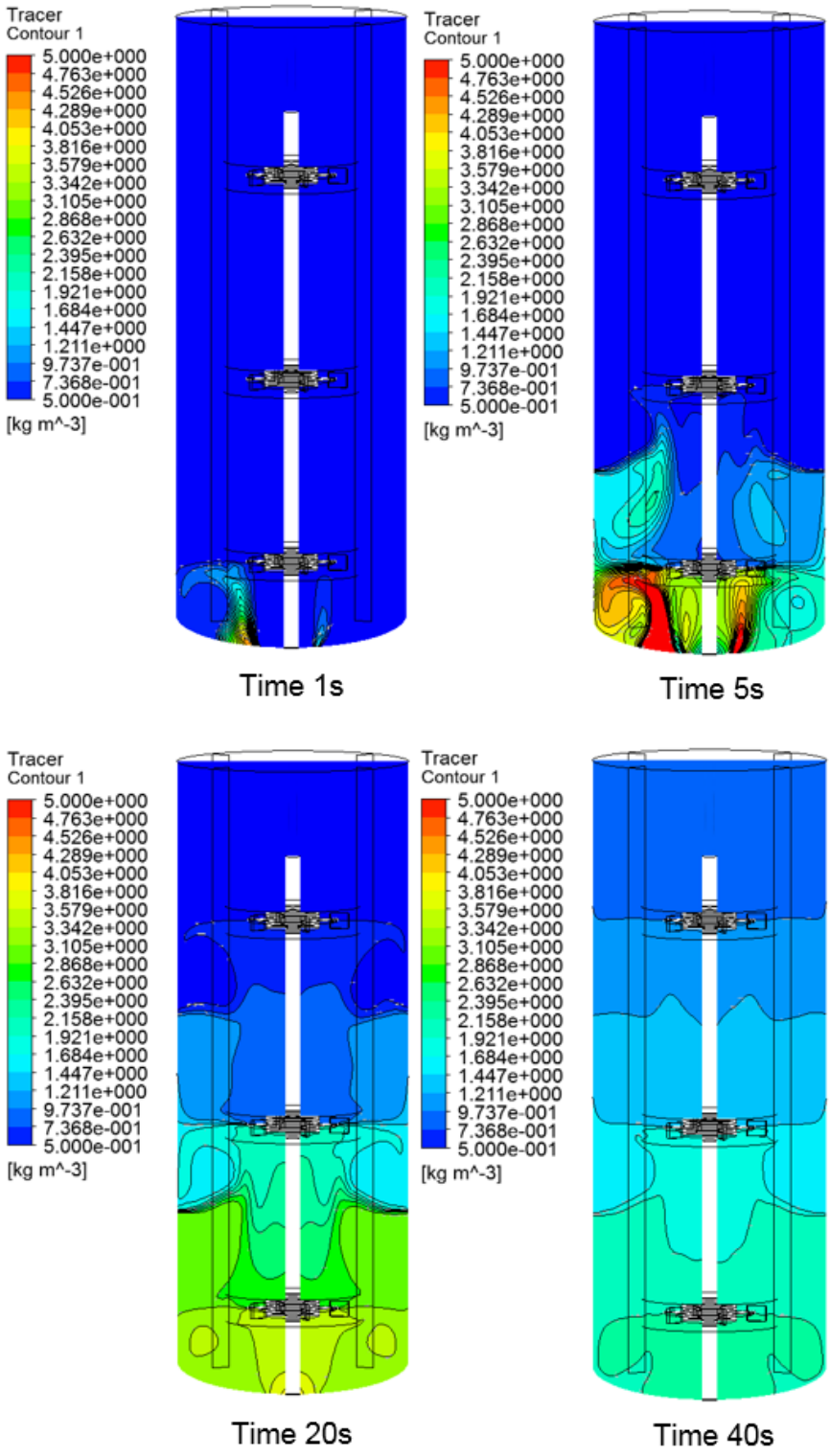


**Figure B.1:** Tracer gradient at 200rpm and bottom pulse.

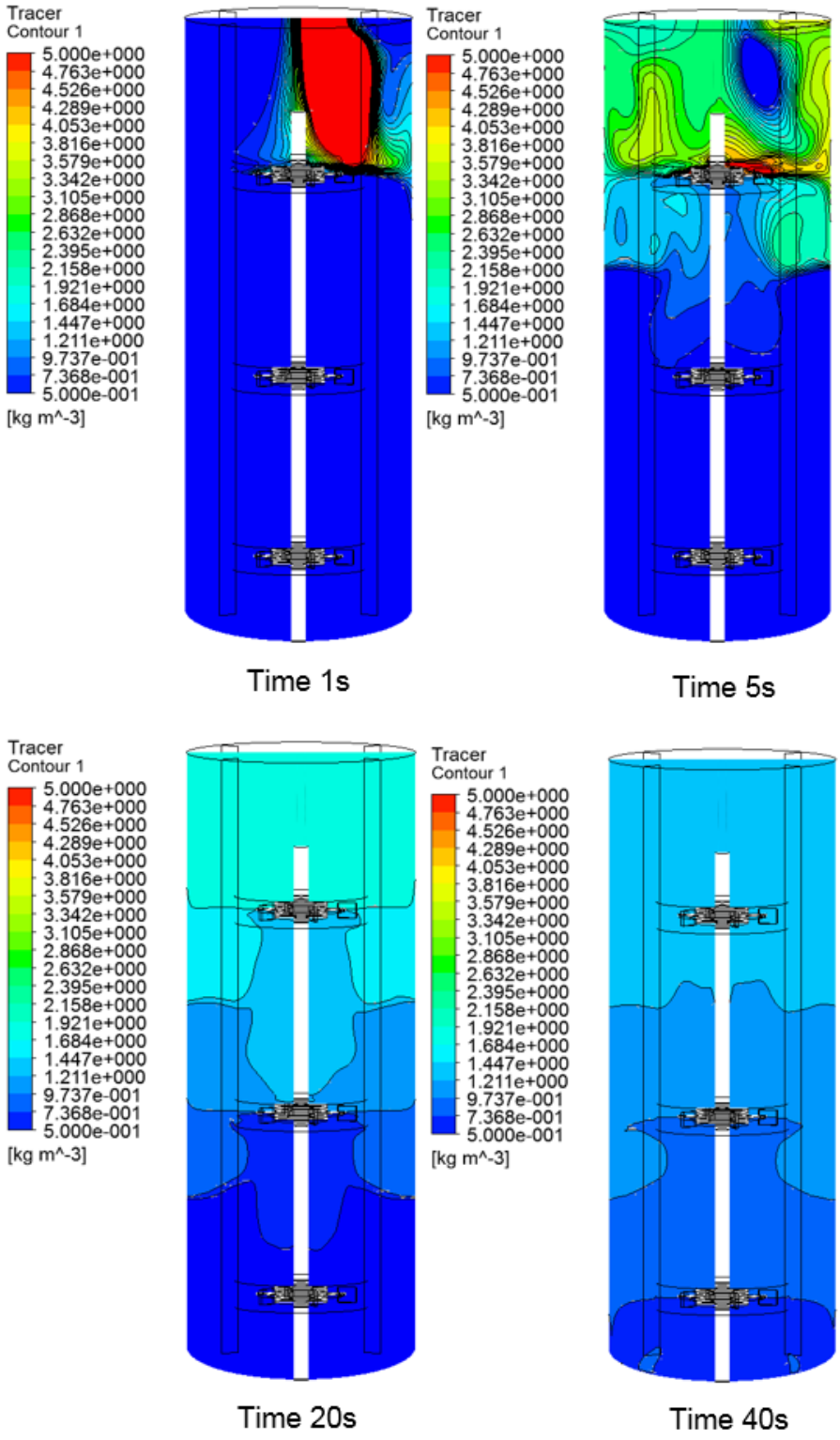


**Figure B.2:** Tracer gradient at 100rpm and top pulse.

APPENDIX C

# Normalized concentration and mixing time of pilot mixing experiments

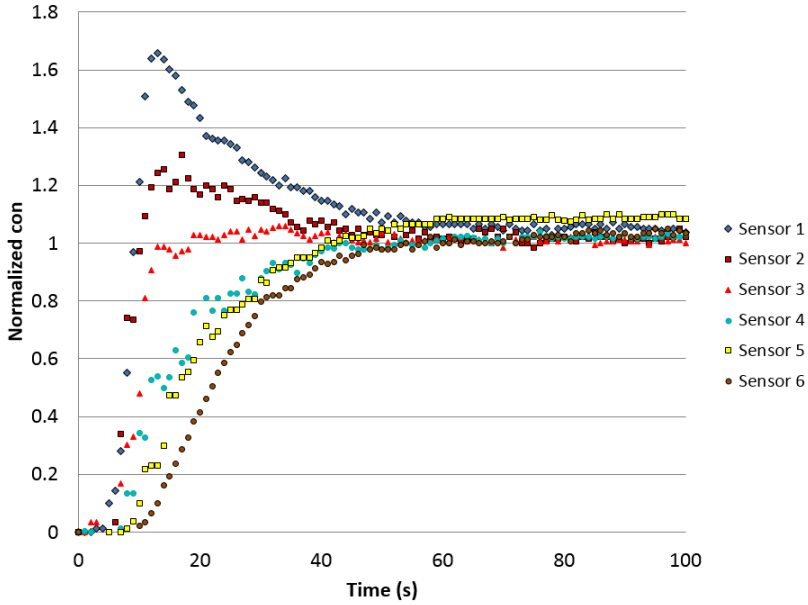


**Figure C.1:** Normalized concentration of pilot mixing experiment 2.

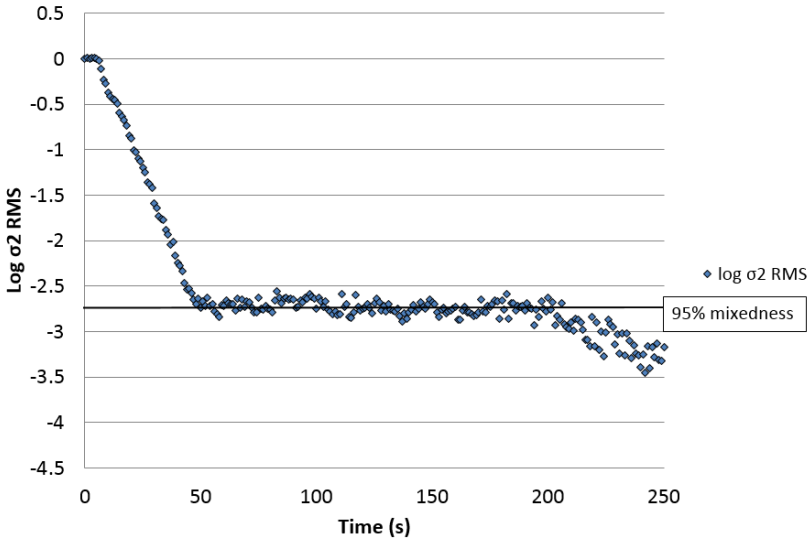


**Figure C.2:** Mixing time of pilot mixing experiment 2.

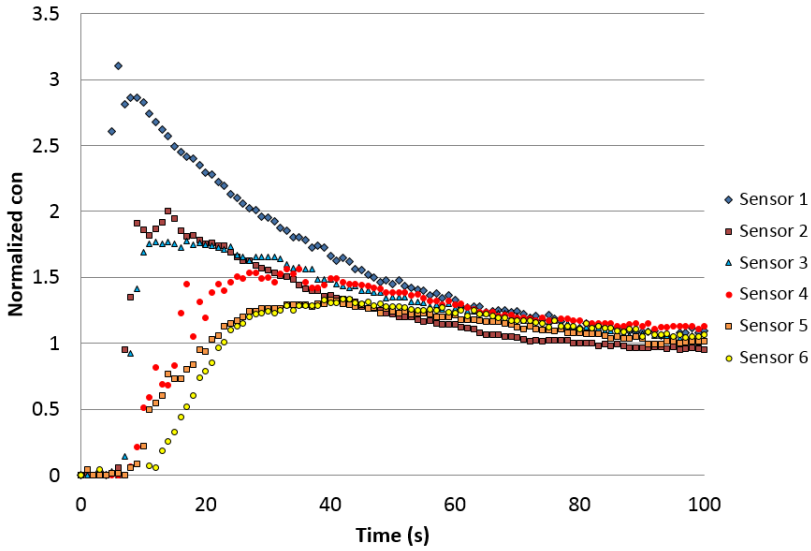


**Figure C.3:** Normalized concentration of pilot mixing experiment 3.

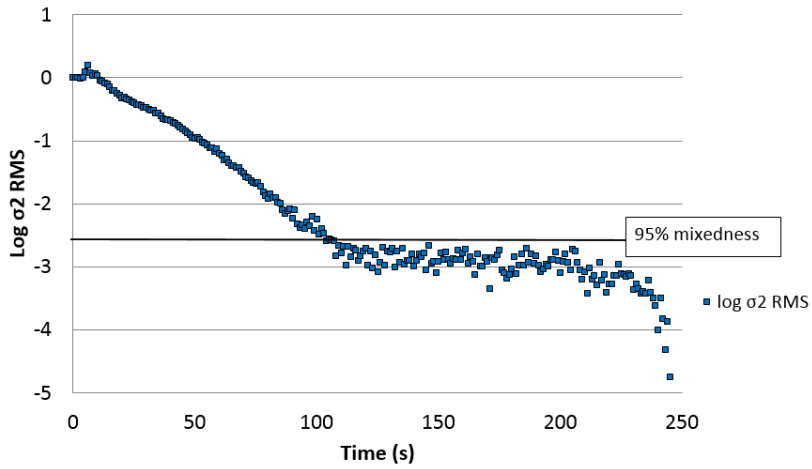


**Figure C.4:** Mixing time of pilot mixing experiment 3.

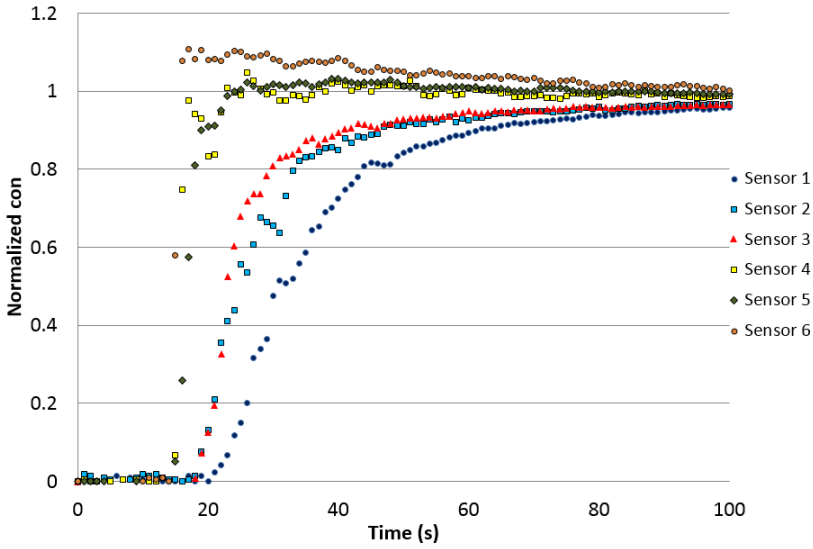


**Figure C.5:** Normalized concentration of pilot mixing experiment 4.

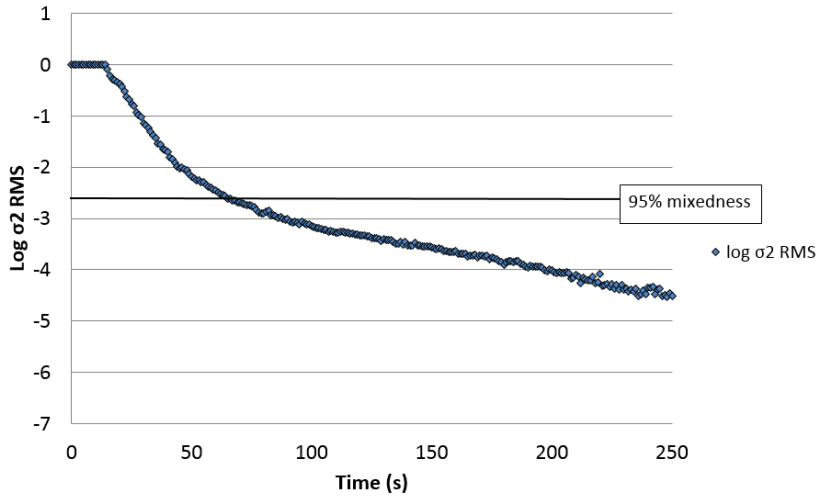


**Figure C.6:** Mixing time of pilot mixing experiment 4.

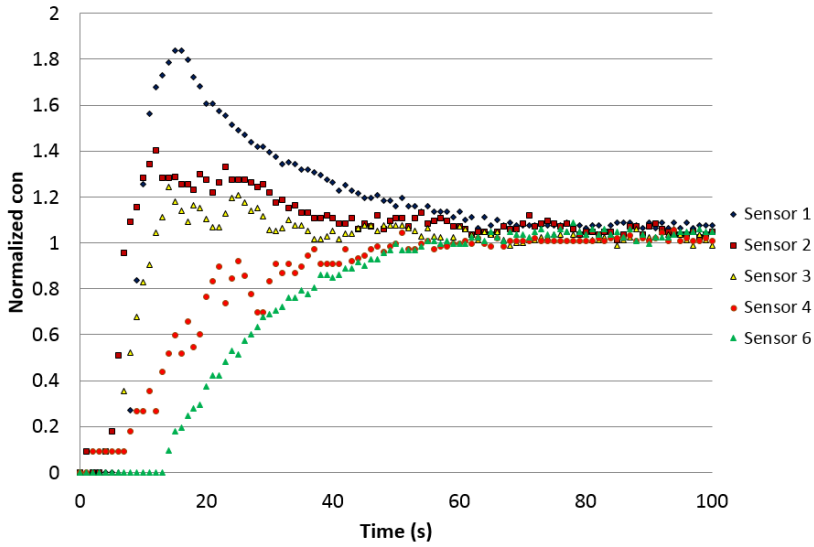


**Figure C.7:** Normalized concentration of pilot mixing experiment 5.

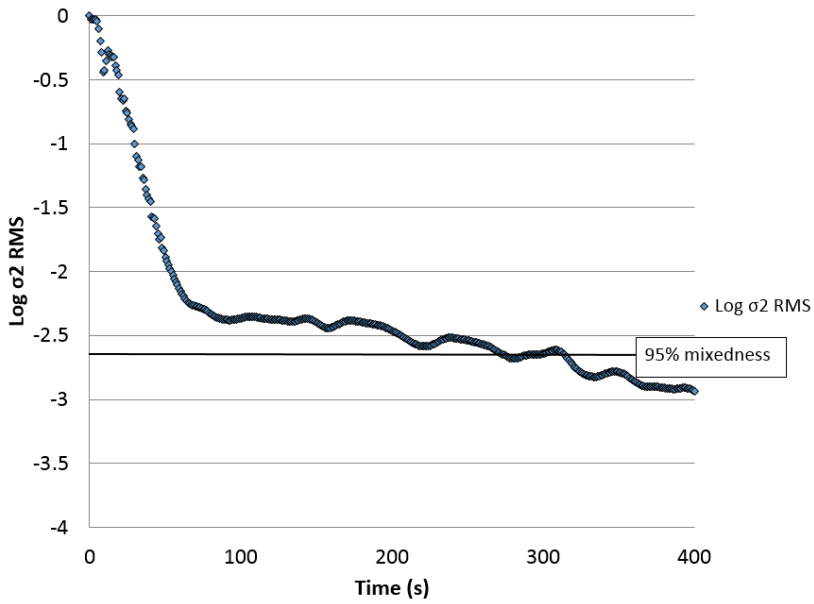


**Figure C.8:** Mixing time of pilot mixing experiment 5.

APPENDIX D

# Growth and consumption diagrams

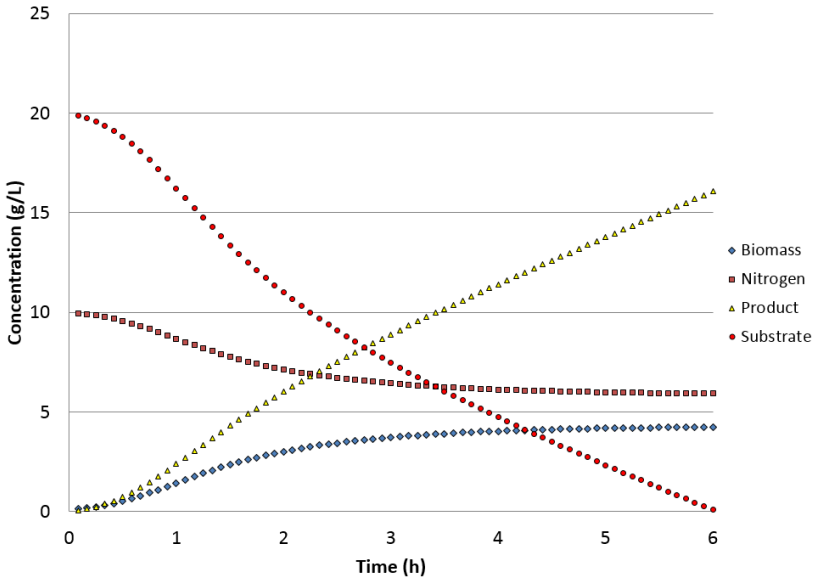


**Figure D.1:** Growth and consumption diagram of a no-flow ideal reactor.

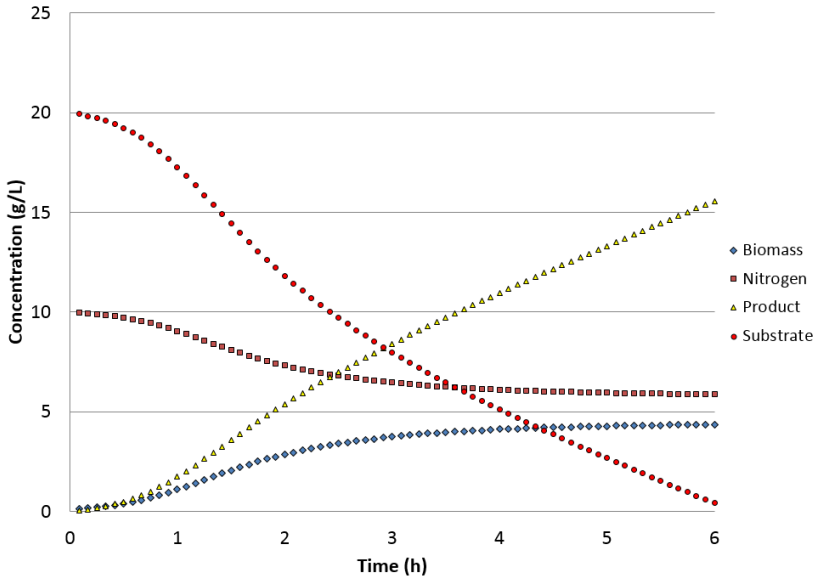


**Figure D.2:** Growth and consumption diagram at 200rpm batch operation.

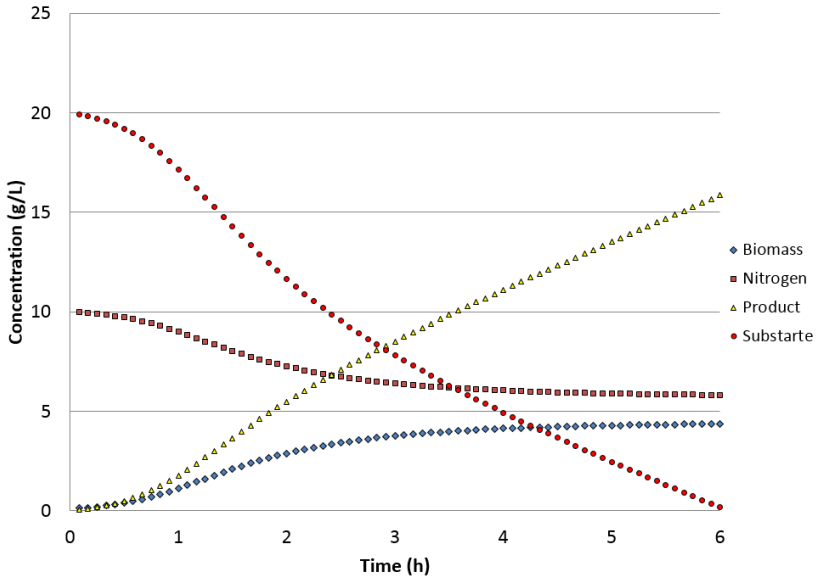


**Figure D.3:** Growth and consumption diagram at 100rpm batch operation.